Examination of modal excitation in few mode fibers

Bachelorarbeit zur Erlangung des akademischen Grades Bachelor of Science [B.Sc.]

verfasst am Institut für Angewandte Optik der Physikalisch Astronomischen Fakultät der Friedrich-Schiller-Universität Jena

von Johannes Wilde

geboren am 1. September 1991 in Göttingen

Matrikelnummer: 125960

Erstgutachter: Prof. Dr. rer. nat. habil. Richard Kowarschik

Zweitgutachter: Dr. rer. nat. Michael Duparré

Contents

Abbreviations

$\#_{\text{modes}}$	number of mutually independent modes guided by a fiber, neglecting the polarization states
$\langle \mid \rangle$	scalar product of radial field distributions
$\overline{}$	average over time
*	complex conjugation
$\vec{\nabla}$	del operator
α	angle of incidence on a fiber front facet
δ_{ij}	Kronecker delta
ζ	free space distance between the phase plate and the fiber input plane
η^p_{lm}	overlap integral describing the mode matching of an incident beam with the mode LP^p_{lm}
$\tilde{\eta}^p_{lm}$	η^p_{lm} normalized to 1 with regard to the maximal incoupled power
$\Theta(x)$	Heaviside step function
λ	wavelength
λ_0	free space wavelength
ρ^p_{lm}	amplitude of c^p_{lm}
$\tilde{\rho}^p_{lm}$	ρ^p_{lm} normalized to 1 with regard to the total incoupled power
σ_0	numerically inscribed beam waist radius of the incident Gaussian beam
φ	angular coordinate in cylinder coordinates
ϕ^p_{lm}	angular component of c^p_{lm}
Φ	phase of a propagating electromagnetic field
ω_0	angular frequency
a	fiber core radius
c^p_{lm}	complex expansion coefficient for the expansion of a beam in LP^p_{lm}-modes
CFM	correlation filter method
E	beam coupled into the fiber
E_{in}	phase shaped irradiating beam
E_{irr}	undisturbed irradiating beam
E^p_{lm}	field distribution of the scalar LP^p_{lm}-modes
E_G	Gaussian beam
$\vec{e}_p$	unit polarization vector
$\vec{e}_r$	unit radial vector
FBG	fiber bragg grating
FMF	few mode fiber

FWHM	full width at half maximum
$J_l(x)$	Bessel function of the first kind and order l at point x
k	propagation constant in propagation direction
$K_l(x)$	modified Bessel function of the second kind and order l at point x
LP-modes	linearly polarized modes
NA	numerical aperture
P_{in}	total power of E_{in}
$P_{\mathrm{incoupled}}$	total power of E
PDMS	polydimethylsiloxane
SLM	spatial light modulator
t	time
V	normalized frequency or V number
w_0	beam waist radius of a Gaussian beam
z_R	Rayleigh length

1. Introduction

Since *Corning Glass Works* [known today as *Corning Incorporated*] produced the first optical fiber featuring an attenuation of less than 20 dB/km in 1970, the use of optical fibers, especially in commercial communications, increased drastically. Also the application in fiber lasers is quite prominent, which - because of it's high optical output power [more than 1 kW [1] in cw-mode], compact and robust setup and high beam quality [1] - is mostly used for material processing. Another application is to use optical fibers as sensors, as they are leightweight, small, sensitive, immune to electromagnetic interferences [2] and [nearly] do not influence the measured system.

Established fiber sensors are for example a "fiber-optic gyroscope", that based on the Sagnac effect can resolve rotations of less than 0.01 °/h [2], a fiber-optic current sensor, that uses the Faraday effect to change the polarization of the guided beam, and a fiber temperature and pressure sensor, in which a fiber inscribed with fiber Bragg gratings does not transmit certain wavelengths. As the latter is the most similar to the setup investigated in this thesis, a very short display of its characteristics shall be given: The reflected wavelength λ_B of a Bragg grating with grating period Λ and effective refractive index n_{eff} of the fiber core at the position of the fiber Bragg grating is $\lambda_B = 2\, n_{\text{eff}}\, \Lambda$. At room temperature n_{eff} is mainly effected by temperature changes and Λ by strain [2]. These sensors are only sensitive at the position of the fiber Bragg grating. It is possible to implement multiple, distinguishable sensor points in one fiber via different multiplexing techniques. To read out the reflected wavelength λ_B either simple setups, that are limited in resolution, or more complex setups, that are expensive and have to be stabilized, are being used [3].

In this thesis a totally different approach was pursued. The principle idea is that external perturbations [e.g. bends, pressure or impurities] of a fiber act differently on different modes guided by the fiber [4, 5]. Modes are distributions of the electromagnetic field, propagating unmodified through the perfect, undisturbed fiber. Using the concept of modes, the complex electromagnetic field distribution in a fiber can be described with only the complex coefficients of each guided mode.

In order to be able to use only an intensity measuring photo diode for the measurement, the modal content coupled into the fiber has to be controlled to ideally one mode only. In order to achieve this, several techniques already exist: For example a very versatile and adaptive setup using a spatial light modulator [SLM] has been employed to excite higher order modes [6, 7] and then investigate the modal dependencies on the bending of the fiber [8]. This setup however is quite expensive and energetically very inefficient. Another approach is to use passive phase plates to shape the incident beam [9]. The energetic efficiency of this setup is much higher and the costs are much lower, the setup however can not be changed easily during the experiment [6, 9].

1 Introduction

The subject of this thesis is the investigation of the efficiency of a setup consisting of a binary phase plate very close to the input facet of an optical fiber [therefore called “monolithic”] with regard to the energetic incoupling as well as the achievable modal purity. Since such a monolithic setup never has been investigated before, this thesis provides a proof of principle for the operation of the modal coupling and will provide an estimation of its capabilities. Additionally this will be compared to the aforementioned approach of free space phase plates.

In section 2 the physical basics needed to understand the setup [like a Gaussian beam, LP-modes and the effect of phase plates on a beam] are described. In section 3 the experimental as well as the numerical setup used in the coming sections will be displayed. The numerical results will then be presented in section 4, the experimental results in section 5.1. The latter will also be compared to the numerical simulations and the parameters, that need to be adjusted, will be pointed out. Finally the comparison with the free space phase plates will be given in section 5.2.

2. Theory

In this sections the basics for understanding the setup used in this investigation will be presented. First a Gaussian beam, as emitted by the laser, will be described. The field distribution derived here, will be used later in section 2.5 again. Then the modes, i.e. stationary field distributions during the propagation, will be derived for weak guiding fibers and it will be shortly indicated how to optically measure their ratio in an optical beam. Finally the basics needed to describe the incoupling of a beam, that was phase shaped by a binary phase plate, and the dependence on the phase shift of the phase plate $\Delta\Phi$ will be presented.

2.1. Gaussian Beam

The commonly emitted field by single mode lasers is a Gaussian beam [10]. Its electric field distribution $\vec{E}$ is derivable from the Maxwell equations, assuming a linear, homogeneous, infinitly extended medium with refractive index n and no free charges or currents. Taking the curl of Faraday's and using Ampère's and Gauss's law one easily obtains the wave equation [11]

$$\vec{\nabla}^2 \vec{E}_G - \frac{n^2}{c^2}\frac{\partial^2}{\partial t^2}\vec{E}_G = 0 \,, \tag{2.1}$$

where $c = 299\,792\,458\,\frac{\mathrm{m}}{\mathrm{s}}$ [12] is the vacuum light velocity and $\vec{\nabla}$ the del operator.

Considering a monochromatic wave with a predominant propagation direction z ["optical axis"] and only small angles to the latter, i.e. the paraxial case, the following ansatz can be made [13]

$$\vec{E}_G = A(x,y,z)\,\mathrm{e}^{\mathrm{i}[kz - \omega_0 t]}\,\vec{e}_p \,; \tag{2.2}$$

here $A(x,y,z)$ denotes an envelope function, (x,y,z) the Cartesian coordinates, t the time, k the propagation constant in z direction, ω_0 the angular frequency and $\vec{e}_p$ the polarization vector.

Neglecting $\frac{\partial^2}{\partial z^2}A$ compared to the other derivatives, i.e. assuming a slowly varying envelope function, one solution normalized in regard to it's total power $P = \int_{\mathbb{R}^2}\left|\vec{E}_G\right|^2 \mathrm{d}x\,\mathrm{d}y = 1$ is

$$\vec{E}_G(\vec{r}) = \frac{\sqrt{2\pi}\,w_0}{\lambda}\,\frac{1}{-z + \mathrm{i}\,z_R}\,\mathrm{e}^{-\mathrm{i}\,k\frac{x^2+y^2}{2[-z+\mathrm{i}\,z_R]} + \mathrm{i}[kz - \omega_0 t]}\,\vec{e}_p \,, \tag{2.3}$$

where the wavelength λ, the Rayleigh length z_R, the beam waist radius w_0 and an arbitrarily oriented unit polarization vector $\vec{e}_p$ are used. This is the transversal fundamental mode for lasers of many types [14].

The beam radius is defined as the radius $w = \sqrt{x^2+y^2}$, at which the respective absolute axial values of $\vec{E}_G$ drop to the $\frac{1}{\mathrm{e}}$-th fraction. It is

$$w(z) = w_0 \sqrt{1 + \left[\frac{z}{z_R}\right]^2} \, . \tag{2.4}$$

The Rayleigh length z_R ist the distance between the beam waist position and where it's cross section area is two times the size; i.e. where $w(z_R) = \sqrt{2}\, w_0$. It is

$$z_R = \frac{\pi}{\lambda} w_0^2 \, . \tag{2.5}$$

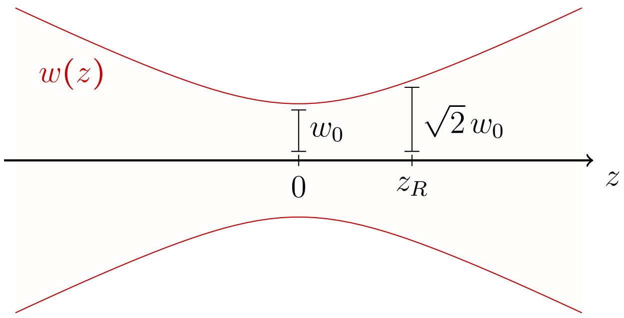

Figure 1: Cross section of a Gaussian beam with propagation direction $\vec{e}_z$.

2.2. Modes in Weakly Guiding Step-Index Fibers

Optical single core fibers in general consist of three very long concentric dielectric cylinders [for a lateral cross section see figure 2]:

1. the core: the innermost, where the light is guided;
2. the cladding: the first outer, which by its lower refractive index leads to the guidance of light in the core;
3. the coating: the outermost, that protects the fiber from destruction by external forces.

The guidance of light in the core of the fiber is understood by total internal reflection at the boundary surface between the core and the cladding. Therefore the index difference

$$\Delta n = n_{\text{core}} - n_{\text{cladding}} \overset{!}{>} 0 \tag{2.6}$$

has to be greater than zero.

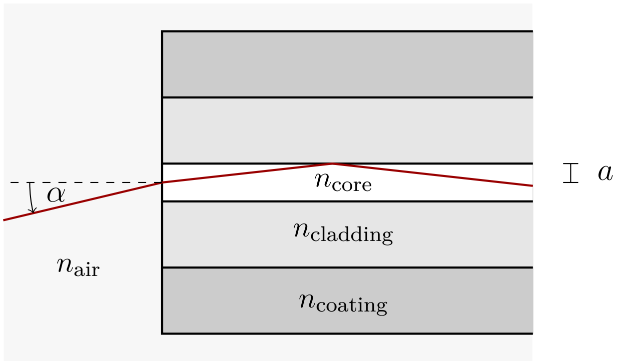

Figure 2: A schematic representation of a cross section of a single core step-index fiber [α denotes the angle of incidence of the light, a the core radius and n_{core}, n_{cladding}, n_{coating} and n_{air} the respective refractive indices].

Starting from a geometrical optic approach, the maximum acceptance angle α [see figure 2] fulfills

$$\mathrm{NA} = n_{\text{air}} \sin(\alpha) = \sqrt{n_{\text{core}}^2 - n_{\text{cladding}}^2}\,, \tag{2.7}$$

where NA is the numerical aperture.

Considering a more sophisticated approach utilizing Maxwell's equations and assuming all the sections of the fiber to be homogeneous, isotropic and linear as well as the index difference Δn to be small [typically in the magnitude of 1×10^{-4}, i.e. "weakly guiding fibers"], one again obtains the wave equation (2.1) [15]

$$\vec{\nabla}^2 \vec{E} - \frac{n^2}{c^2} \frac{\partial^2}{\partial t^2} \vec{E} = 0\,, \tag{2.8}$$

however now the refractive index n is radially dependent: It is $n = n_{\text{core}}$ inside the core and $n = n_{\text{cladding}}$ outside the core. I.e. the cladding is assumed to expand to infinity; as for guided modes in this paraxial case a quite strong decay of the $\vec{E}$-field in the cladding is expected, this only induces a very small error.

With these assumptions, choosing z as the propagation direction for a monochromatic wave of angular frequency ω_0 and propagation constant β and using cylindrical coordinates (r, φ, z), which are most suitable for this problem, the ansatz

$$\vec{E} = E_0\, \mathcal{R}(r)\, \mathcal{P}(\varphi)\, \mathrm{e}^{\mathrm{i}[\beta z - \omega_0 t]}\, \vec{e}_r \tag{2.9}$$

can be made [15]. It depicts E_0 an arbitrary amplitude, t the time and $\vec{e}_r$ a transversally arbitrarily oriented, unit polarization vector.

As (2.8) has no effect on the polarization state, the direction of $\vec{e}_r$ is independently eligible. By choosing two orthonormal vectors in the transversal plane, all possible polarization states can be described using a superposition of these two.

Regarding the remaining problem, i.e. only the scalar one, one obtains from (2.8) and (2.9) by separating the variables the following two equations [$l \in \mathbb{C}$]:

$$\frac{\partial^2}{\partial\varphi^2}\mathcal{P}(\varphi) + l^2\mathcal{P}(\varphi) = 0 \quad , \quad r^2\frac{\partial^2}{\partial r^2}\mathcal{R}(r) + r\frac{\partial}{\partial r}\mathcal{R}(r) + [[k^2 - \beta^2]r^2 - l^2]\mathcal{R}(r) = 0 \quad . \tag{2.10}$$

From the smoothness of the solutions and φ being 2π-periodic, the periodicity of the azimuthal component $\mathcal{P}(\varphi)$ follows. Therefore with l being a positive integer or 0 one obtains all possible solutions.

The right equation has, after rescaling r, the form of Bessel's differential equation [15]. As only squared integrable and convergent functions are solutions of interest, it follows

$$k_{\text{core}} \geq \beta \geq k_{\text{cladding}} \ , \tag{2.11}$$

where k_0 is the free space propagation constant and $k_{\text{core}} = n_{\text{core}}\, k_0$ and $k_{\text{cladding}} = n_{\text{cladding}}\, k_0$ are the values in the respective medium.

With

$$u = a\sqrt{k_{\text{core}}^2 - \beta^2} \qquad \text{and} \qquad w = a\sqrt{\beta^2 - k_{\text{cladding}}^2} \tag{2.12}$$

one obtains from the smoothness of the derivative of the E-field at $r = a$ [11]

$$-\frac{J_l(u)}{u\, J_{l-1}(u)} = \frac{K_l(w)}{w\, K_{l-1}(w)} \ . \tag{2.13}$$

It is J_l the Bessel function of the first kind and order l and K_l the modified Bessel function of the second kind [also called modified Hankel function or Macdonald function] and order l.

This is only solveable for discrete u and w. As for each $l \in \mathbb{N}_0$ there can exist several solutions (u, w), they are named (u_{lm}, w_{lm}) , $m \in \mathbb{N}$ enumerating them. To illustrate this, in figure 3 both sides of (2.13) are plottet for $l = 0$ and the intersections are enumerated with the respective m-value.

Correspondingly only discrete β_{lm} are possible.

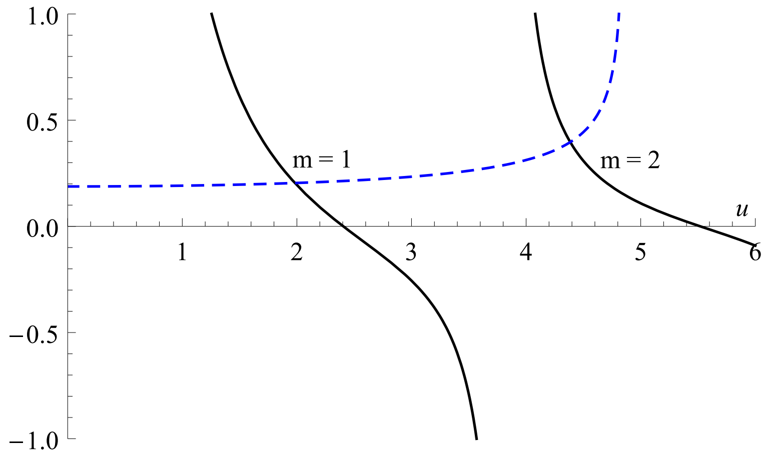

Figure 3: Plot of the left-hand side [solid] and the right-hand side [dashed] of (2.13) for $V = 4.847$ [see (2.15)] and $l = 0$ over u.

Now the physically relevant eigensolutions in the paraxial approximation, disregarding the polarization states, are:

$$E_{lm}^{p} = E_0 \left\{ \begin{array}{c} \dfrac{1}{J_l(u_{lm})} J_l(u_{lm}\dfrac{r}{a}) \\ \dfrac{1}{K_l(w_{lm})} K_l(w_{lm}\dfrac{r}{a}) \end{array} \right\} \cos(l\varphi + \varphi_0^p)\, \mathrm{e}^{\mathrm{i}[\beta_{lm} z - \omega_0 t]} \quad \begin{array}{l} , 0 \le r < a \\ , a \le r \end{array} \quad . \tag{2.14}$$

It is $p \in \{e, o\}$, without loss of generality $\varphi_0^e = 0$ [as the cosine is even] and $\varphi_0^o = \dfrac{\pi}{2}$ [as the sine is odd], J_l inside the core $[0 \le r < a]$ and K_l outside the core $[r \ge a]$. The normalization constants $\dfrac{1}{J_l(u_{lm})}$ and $\dfrac{1}{K_l(w_{lm})}$ respectively ensure the continuity of the solution. These modes are called LP-modes, because they are linearly polarized.

The square root of the quadratic sum of u_{lm} and w_{lm} yields the normalized frequency [or V number] [16]

$$V = \sqrt{u_{lm}^2 + w_{lm}^2} = k_0\, a\, \mathrm{NA} \ . \tag{2.15}$$

For V greater than 5 the total number of mutually independent modes guided by the fiber [neglecting the polarization states] can be approximated by [16, 17]

$$\#_{\text{modes}} \approx \frac{V^2}{4} \ . \tag{2.16}$$

The LP-modes are orthonormal; i.e. :

$$\left\langle E^p_{lm} \,\middle|\, E^q_{no} \right\rangle = \int_{\mathbb{R}^2} \mathrm{d}A \, E^{p\,*}_{lm} \, E^q_{no} = \delta_{ln} \, \delta_{mo} \, \delta_{pq} \, , \tag{2.17}$$

δ_{ij} depicting the Kronecker delta and the asterix * complex conjugation.

Thus every guided optical field distribution E is expandable in a series of these LP-modes:

$$E = \sum_{l,m,p} c^p_{lm} E^p_{lm} \qquad , \tag{2.18}$$

where

$$c^p_{lm} = \rho^p_{lm} \, \mathrm{e}^{\mathrm{i}\,\phi^p_{lm}} = \left\langle E^p_{lm} \,\middle|\, E \right\rangle \in \mathbb{C} \quad , \quad \rho^p_{lm} \in \mathbb{R}_{\geq 0} \, , \; \phi^p_{lm} \in [0, 2\pi) \tag{2.19}$$

are the complex expansion coefficients.

2.3. Correlation Filter Method

As with standard light sensors [photo-resistors, photo-diodes or cameras] only the timely averaged intensity $\overline{|E|^2}$ is directly measurable, c^p_{lm} can't be directly determined. [The overbar $\overline{}$ stands for the average over time.]

But by considering the following transmission function for an optical filter [18]

$$T(\vec{\xi}) = \sum_{l,m,p} E^{p\,*}_{lm} \, \mathrm{e}^{\mathrm{i}\,\vec{\nu}^{\,p}_{lm}\vec{\xi}} + \sum_{\substack{l,m,p \\ (l,m,p) \neq (f,g,h)}} \frac{1}{\sqrt{2}} \left[E^{h\,*}_{fg} + E^{p\,*}_{lm} \right] \mathrm{e}^{\mathrm{i}\,\vec{\nu}'^{\,p}_{lm}\vec{\xi}} + \sum_{\substack{l,m,p \\ (l,m,p) \neq (f,g,h)}} \frac{1}{\sqrt{2}} \left[E^{h\,*}_{fg} + \mathrm{i} \, E^{p\,*}_{lm} \right] \mathrm{e}^{\mathrm{i}\,\vec{\nu}''^{\,p}_{lm}\vec{\xi}} \, , \tag{2.20}$$

where $\vec{\xi} \in \mathbb{R}^2$ names the coordinates in the filter plane and $\vec{\nu}^{\,p}_{lm} \in \mathbb{R}^2$, $\vec{\nu}'^{\,p}_{lm} \in \mathbb{R}^2$ and $\vec{\nu}''^{\,p}_{lm} \in \mathbb{R}^2$ are all different spatial frequencies, one obtains in the Fourier plane [either in the far field or by employing a single lense in a $2f$-setup behind the filter], assuming $\vec{\nu}^{\,p}_{lm}$, $\vec{\nu}'^{\,p}_{lm}$ and $\vec{\nu}''^{\,p}_{lm}$ are distant enough from each other, the following values at the respective spatial frequencies:

$$\begin{aligned}
\vec{\nu}^{\,p}_{lm} \quad &: \qquad I^p_{lm} = \overline{\left|c^h_{fg}\right|^2} = \rho^{p\;2}_{lm} \, , \\
\vec{\nu}'^{\,p}_{lm} \quad &: \qquad I'^p_{lm} = \tfrac{1}{2}\overline{\left|c^h_{fg} + c^p_{lm}\right|^2} = \tfrac{1}{2}\left[\rho^{h\;2}_{fg} + \rho^{p\;2}_{lm} + 2\,\rho^h_{fg}\,\rho^p_{lm}\,\overline{\cos(\phi^h_{fg} - \phi^p_{lm})} \right] \, , \\
\vec{\nu}''^{\,p}_{lm} \quad &: \qquad I''^p_{lm} = \tfrac{1}{2}\overline{\left|c^h_{fg} + \mathrm{i}\,c^p_{lm}\right|^2} = \tfrac{1}{2}\left[\rho^{h\;2}_{fg} + \rho^{p\;2}_{lm} + 2\,\rho^h_{fg}\,\rho^p_{lm}\,\overline{\sin(\phi^h_{fg} - \phi^p_{lm})} \right] \, .
\end{aligned} \tag{2.21}$$

E^h_{fg} is an arbitrarily choosable reference mode for the phase measurement. It is obvious, that for meaningful I'^p_{lm} and I''^p_{lm} ρ^h_{fg} has to be nonzero.

The transformation into the Fourier plane thereby performs exactly the scalar product from (2.17) at each of the above mentioned spatial frequencies for the corresponding mode.

In case of a coherent E-field, the phase-relations are found by

$$\phi^p_{lm} - \phi^h_{fg} = -\operatorname{atan}\left(\frac{2\,I''^{\,p}_{lm} - I^h_{fg} - I^p_{lm}}{2\,I'^{\,p}_{lm} - I^h_{fg} - I^p_{lm}}\right) \qquad \in (-\pi, \pi] \quad . \tag{2.22}$$

By inscribing the transmission function $T(\vec{\xi})$ into a computer generated hologram [CGH] and evaluating the intensities at the spatial frequencies, the full modal content of a linearly polarized, coherent beam can be determined in real-time.

Additionally considering the two possible transversal polarization states of each previously described LP-mode, the parameters needed to describe the linearly polarized, coherent electric field $\vec{E}$ become twice as many.

2.4. Beamshaping

In order to control the excitation of particular modes inside an optical fiber, several approaches have already been made: As one approach only the phase profile of the incident beam has been shaped. Therefore several experimental realizations have been investigated already [e.g. a passive phase plate in free space [19, 20], a spatial light modulator [6–9] or a phase profile directly machined on the fiber tip [21]]. In an other approach the phase and the amplitude profile of the incident beam have been modified [9]. All these techniques show different characteristics.

One quantity, that describes the coupling efficiency of the incoming electric field E_{in} to each LP-mode E^p_{lm}, is the following overlap integral [22]:

$$\eta^p_{lm} = \frac{\left|\int E^{p\,*}_{lm} E_{\text{in}}\,\mathrm{d}A\right|^2}{\int \left|E^p_{lm}\right|^2 \mathrm{d}A \int \left|E_{\text{in}}\right|^2 \mathrm{d}A} \tag{2.23}$$

If η^p_{lm} is dependent on several variables [for notation they shall be combined to a single vector $\vec{x}$ at this moment] and if $\vec{x}_{\max}$ depicts the position where $\sum\limits_{l',m',p'} \eta^{p'}_{l'm'}(\vec{x}_{\max})$ is maximal, then the following two normalized quantities shall be defined:

$$\tilde{\eta}^p_{lm}(\vec{x}) = \frac{\eta^p_{lm}(\vec{x})}{\sum\limits_{l',m',p'} \eta^{p'}_{l'm'}(\vec{x}_{\max})} \qquad \text{and} \qquad \tilde{\rho}^{p\,2}_{lm}(\vec{x}) = \frac{\eta^p_{lm}(\vec{x})}{\sum\limits_{l',m',p'} \eta^{p'}_{l'm'}(\vec{x})} \ . \tag{2.24}$$

$\tilde{\eta}_{lm}^{p}$ describes the coupling efficiency, normalized to a maximum value of 1, and $\tilde{\rho}_{lm}^{p\,2}$ describes the relative modal energy coupled into the beam for each $\vec{x}$.

If the total transversal power $P_{\text{incoupled}} = \int |E|^2 \,\mathrm{d}A$ inside the fiber is normalized to 1, then it is

$$\tilde{\rho}_{lm}^{p\,2} = \rho_{lm}^{p\,2}. \tag{2.25}$$

Obviously, by modulating the amplitude and phase distribution of the irradiating beam E_{irr} to obtain an incident beam at the fiber tip E_{in} exactly adapted to the desired mode E_{st}^{v}, the overlap integral η_{lm}^{p} becomes maximal with respect to the desired mode $[\eta_{st}^{v} \to 1]$ and minimal with respect to the undesired modes $[\eta_{lm}^{p} \to 0 \;,\; (l,m,p) \neq (s,t,v)]$. The same holds for the relative power of each mode inside the fiber $\tilde{\rho}_{lm}^{p\,2}$ $[\tilde{\rho}_{st}^{v\,2} \to 1$ and $\tilde{\rho}_{lm}^{p\,2} \to 0 \;, (l,m,p) \neq (s,t,v)]$.

However by shaping the amplitude profile, a lot of the initial power of E_{irr} is lost. At least if the irradiating beam is not already very similar to the desired mode, like a Gaussian beam and an LP_{01}-mode. This is understandable if one considers that the point of maximum power of the desired mode might be where the intensity of E_{irr} is small and that the intensity at every other point has to be attenuated, so its proportion to the maximum power is right.

As for lower order LP-modes the phase profile is “the most prominent differentiator between modes” [9] and via pure phase shaping no power loss from E_{irr} to E_{in} is induced, for FMFs mere phase shaping seems the more reasonable approach.

The insertion loss though, not because of reflections at the fiber input plain, but because of the missing amplitude profile adjustment, will be bigger. For a quantitative statement the experimental setup hence was first investigated by numerical simulations of the coupling process, as shown in section 4.

The phase plates used in this study consist of binary phase profiles, adjusted to the phase profiles of the desired modes [see section 2.5 on page 11 figure 5 and section 4.1 on page 15 figure 9].

The phase shift is induced via an optical element with refractive index n_{ph} in a medium with refractive index n. If the thickness of this element varies by d [see figure 4], the induced phase shift is

$$\Delta\Phi = [n_{\text{ph}} - n]\frac{d}{\lambda_0}2\pi \;, \tag{2.26}$$

where λ_0 is the free space wave length of E_{irr}.

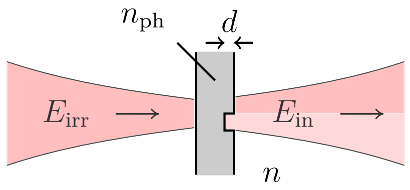

Figure 4: Scheme of the effect of a phase plate on the phase profile of a Gaussian beam at its waist.

2.5. Phase Shift $\Delta\Phi$

From formula (2.14) one sees, using cylindrical coordinates (r, φ, z), that the transversal phase profile of the LP-modes E^p_{lm} for $m = 0$ is proportional to $\cos(l\varphi + \varphi_0)$. Accordingly the phase plate for the excitation of the LP_{01}-mode $\boxed{0}$ shows only one section of constant phase shift $\Delta\Phi$. The phase plate for excitation of LP_{11} $\boxed{1}$ is divided in two sections $[\varphi \in [0°, 180°)$ and $\varphi \in [180°, 360°)]$ with each constant phase shifts 0° or $\Delta\Phi$ respectively. The phase plate for the excitation of the LP_{21}-mode $\boxed{2}$ is divided in four sections $[\varphi \in [0°, 90°), \varphi \in [90°, 180°), \varphi \in [180°, 270°)$ and $\varphi \in [270°, 360°)]$ with alternating phase shifts 0° and $\Delta\Phi$. Their phase shift profiles are shown in figure 5.

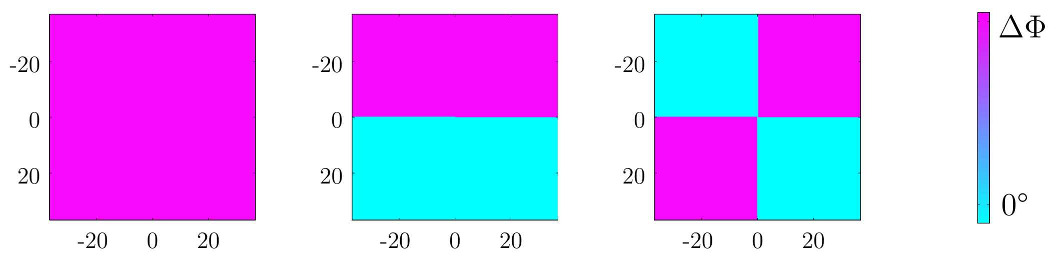

Figure 5: Transversal phase plate phase shift profiles [$\boxed{0}$, $\boxed{1}$, $\boxed{2}$]; dimensions in µm.

By considering the symmetry of the phase plates and the LP-modes, it is evident that for $\Delta\Phi = 180°$ a Gaussian beam E_G phase shifted by phase plate $\boxed{l}$ only couples in LP-modes E^p_{lm} with the same l.

IF $\Delta\Phi$ different is to 180° for a phase plate $\boxed{l}$, then the phase shifted beam E_{in} can be described by superposing an unperturbed beam E_{irr} of different relative amplitude $\tilde{\rho}_0$ with a perfectly phase shifted one of respective relative amplitude $\tilde{\rho}_l$. The amount of energy in each of the superposed beams can be calculated by an overlap integral similar to $\tilde{\eta}^p_{lm}$ [see page 9] and leads the same result for all phase profiles corresponding to LP-modes with $m = 0$. As an example for LP_{11} it is [E_G normalized with regard to its power to 1]

$$\tilde{\rho}_0^2 = \left| \int_{0\,\mathrm{m}}^{\infty\mathrm{m}} \int_{0°}^{360°} E_G^* \left[E_G \left[\Theta(\varphi - 180°) + \Theta(180° - \varphi)\, \mathrm{e}^{\mathrm{i}\,\Delta\Phi} \right] \right] \mathrm{d}r\, \mathrm{d}\varphi \right|^2 = \frac{1}{2}[1 + \cos(\Delta\Phi)]\,; \tag{2.27}$$

with $\Theta(x)$ being the Heaviside step function. Because $\tilde{\rho}_0^2 + \tilde{\rho}_l^2 = 1$, it follows easily that

$$\tilde{\rho}_l^2 = \frac{1}{2}\,[1 - \cos(\Delta\Phi)]\,. \tag{2.28}$$

All other $\tilde{\rho}_n^2$, $n \neq l$ and $n \neq 0$ are, when using a phase plate $\boxed{l}$, zero; this is obvious by considering again the symmetry of the phase profiles.

3. Experimental Setup

A scheme of the experimental setup is shown in figure 6. The laser source was a Nd:YAG laser that emitted a Gaussian beam [beam quality factor $M^2_{\text{eff}} = 1.21$] at a single wavelength of 1064 nm. The beam was coupled by a microscope objective [$f = 10.0$ mm] into the used fiber [*Nufern LMA-GDF-25/250-M*, douple clad, core radius $a = 12.5\,\mu\text{m} \pm 1.5\,\mu\text{m}$, $NA = 0.065 \pm 0.005$], at which's front facet a binary phase plate passively shaped the incident beam. These phase plates were manufactured specially for this experiments at the Institute of Photonic Technology Jena [IPHT Jena] by making a mold in polydimethylsiloxane [PDMS] from a silicon structure. Because for the refractive index of PDMS at the used wavelength at first only a rough estimation [$n_{\text{PDMS}} \approx 1.5$] existed, an estimated thickness difference of $d = 1064$ nm was manufactured. On each of the phase plates several copies of one of the structures shown in figure 7 were inscribed. The phase plates were then fixated by adhesive forces, centered on a metal cylinder, in which's center one fiber end stuck. This way the free space distance between fiber input facet and phase plate was minimized. This setup will be called "monolithic".

A second microscope objective with a focal length of $f = 25.4$ mm together with a lense with a focal length of $f = 375$ mm in a $4f$-setup magnified the beam after the fiber, in order to adjust the beam size to the hologram in the correlation filter. The correlation filter was fabricated as a binary amplitude hologram at the IPHT Jena by laser lithography. The technique used to encode the transmission function was the one suggested by Lee [23], as it features the better signal to noise ratio compared to Lohmann holograms [24]. The hologram consists of 512×512 Lee cells, that each are $16\,\mu\text{m} \times 16\,\mu\text{m}$ wide and show a smallest structure of 700 nm. The second lense [$f = 180$ mm] fourier transformed the signal of the correlation filter in a $2f$ setup onto a camera [1/1.8″ CCD, 1600×1200 pixels, each $4.4\,\mu\text{m} \times 4.4\,\mu\text{m}$].

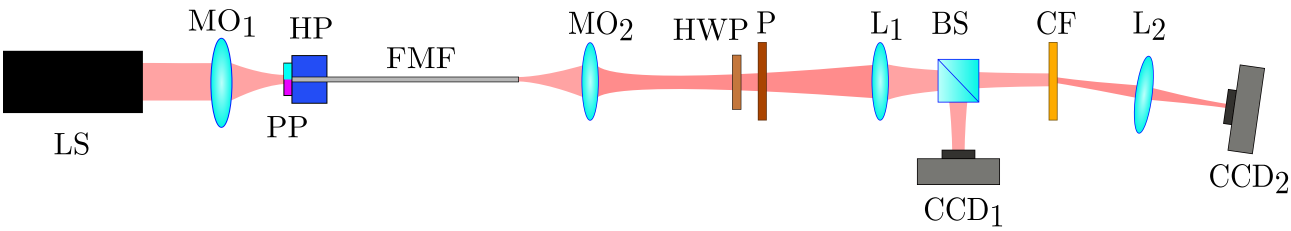

Figure 6: Scheme of the experimental setup [LS - laser source, $MO_{1,2}$ - microscope objectives, PP - phase plate, HP - Hexapod, FMF - few mode fiber, HWP - $\frac{3\lambda}{2}$ waveplate, P - polarizer, $L_{1,2}$ - lenses, BS - beam splitter, $CCD_{1,2}$ - cameras, CF - correlation filter].

By rotating the half wave plate in front of the Glan-Thompson prism, the polarization under investigation could be chosen without having to rotate the prism. Thereby the prismatic deviations were minimized [25]. The camera CCD_1 captured the nearfield emitted by the fiber, in order to be able to control the quality of the reconstruction via the correlation filter method [CFM].

Figure 7: Excerpts of the actual transversal thickness profiles of the phase plates used for the monolithic setup.

For the numerical simulations the modal analysis of the incoupled beam E could be performed numerically, i.e. without the CFM. Therefore, as shown in figure 8, an irradiating Gaussian beam E_{irr} was simulated, that was phase shaped by a phase plate to the beam E_{in} incident on the fiber, which then coupled into the fiber to the guided beam E. The distance between phase plate and fiber input facet will be called ζ.

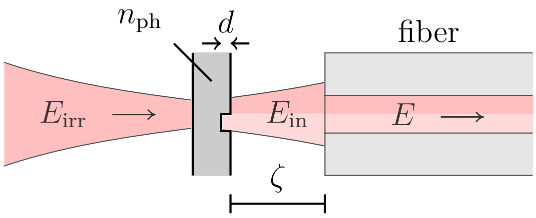

Figure 8: Scheme of the effect of a phase plate on the phase profile of a Gaussian beam at its waist.

Additionally σ_0 will be used. This parameter describes the inscribed beam waist radius of the incident Gaussian beam. The purpose of using σ_0 instead of w_0 is to emphasize that the Gaussian beam, after beeing modified by the phase plate, does not propagate the same way as without beeing modified. For the simulations the undisturbed beam waist was always assumed to be at the fiber input plane.

4. Numeric

In this section the numerical results concerning the modal coupling efficiency depending on the beam waist radius of the incident beam σ_0 [4.2], the free space distance between the phase plate and the fiber input plane ζ [4.3] and the transversal misalignement of the incident beam [4.4] will be displayed.
At first though the outsets used for the simulations will be described.

4.1. Numerical Setup

The fiber *Nufern LMA-GDF-25/250-M*is a step index fiber with a cylindrical core with an assumed radius of $a = 12.25\,\mu\text{m}$ and refractive index $n_{\text{core}} = 1.4515$. Because of the strong decay of the guided mode's power in the cladding, no other regions outside of it were numerically considered. The cladding was assumed to be undoped glass and therefore $n_{\text{cladding}} = 1.4500$.

The guided *LP*-modes were determined numerically via a scalar finite difference modesolver [26] and are shown in figure 9.

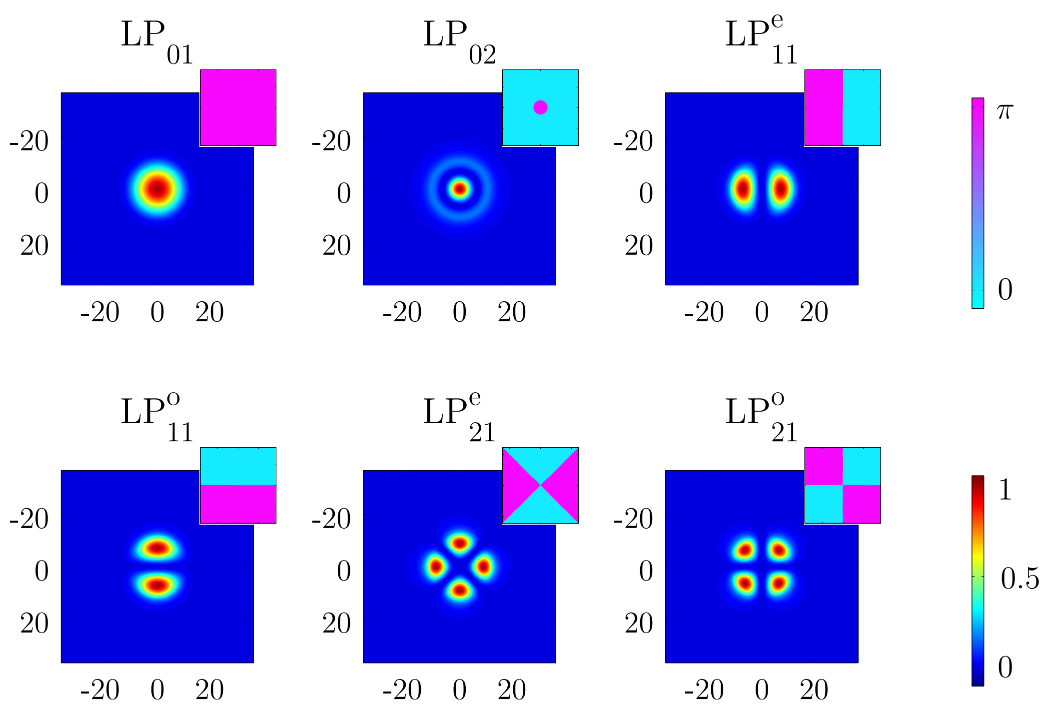

Figure 9: Amplitude and phase [insets] profile of the six guided *LP*-modes in the *Nufern LMA-GDF-25/250-M* of wavelength $\lambda = 1064\,\text{nm}$ calculated numerically; dimensions in µm.

As mentioned earlier, the phase-profile, as displayed in the insets in figure 9, is a very “prominent differentiator between [these lower order] modes” [9].

The phase plates used for the simulation were already described in section 2.5 on page 11 and turn out to be in very good agreement with the numerical results for the phase profiles of the LP-modes shown in the insets in figure 9.

It should be noted, that all of the following calculations have been made, distinguishing between even and odd LP-modes. Yet, considering the perfect azimuthal symmetrie of the assumed fiber profile, it is obvious that the rotation of the phase plate and the arbitrariness of the orientation of the even and odd modes make this unnecessary. Only if one considerd symmetry-breaking disturbances on the fiber, this would be required. This however is not subject of this study.

Additionally in real FMFs mode mixing mainly between the two even and odd orientations of one LP-mode and simultaneously between the orthogonal polarization states occurs [“modal birefringence” and “random coupling” [27]], which makes the knowledge about the excited LP-mode in respect to it’s orientation useless, as the modal content might have changed at another posititon in the fiber.
Thus only the mode group resolved modal contents of $E_{\text{incoupled}}$ are displayed in the following. One obtains these by

$$\eta_{lm} = \sum_{p\in\{e,o\}} \eta_{lm}^{p} \quad , \quad \tilde{\eta}_{lm} = \sum_{p\in\{e,o\}} \tilde{\eta}_{lm}^{p} \quad , \quad \rho_{lm}^{2} = \sum_{p\in\{e,o\}} \rho_{lm}^{p\;2} \quad \text{and} \quad \tilde{\rho}_{lm}^{2} = \sum_{p\in\{e,o\}} \tilde{\rho}_{lm}^{p\;2} \quad . \tag{4.1}$$

4.2. Beam Waist Radius σ_0

First the dependency of the excited mode spectrum on the beam waist radius of the incoming Gaussian beam σ_0 was investigated, neglecting all other possible errors or misalignments. Therefore a Gaussian beam was calculated numerically at its waist, scaled for different σ_0 and phase shifted in its transversal profile corresponding to the phase plates shown in figure 5 on page 11. Then the overlap with each of the modes shown in figure 9 was calculated. In figures 10, 11 and 12 the dependencies for the different phase plates are shown.

The results for the phase plate $\boxed{0}$, which is equivalent to using no phase plate at all, in figure 10 show, in accordance with the azimuthal symmetry of the fiber and the incident beam, that only the azimuthally symmetric LP_{01}- and LP_{02}-mode are excited.

The beam waist radius with maximal energy coupled into the LP_{01}-mode in this setup is $\sigma_{\text{max}} = 9.97\,\mu\text{m}$. However, at this size the energy coupled into the fiber is not maximal [99.3 % instead of 99.6 %], because the radii of maximal coupling efficiency are different for all modes. That more than 99.3 % are coupled into the LP_{01}-mode is due to the resemblance of a gaussian beam with the LP_{01}-mode.

The fact that there is only one maximum of incoupling efficiency should be noted; by knowing that there are no local maxima beside this one, the experimental adjustment with phase plate $\boxed{0}$ for LP_{01} in regard to the beam size σ_0 is simplified to locating an intensity maximum.

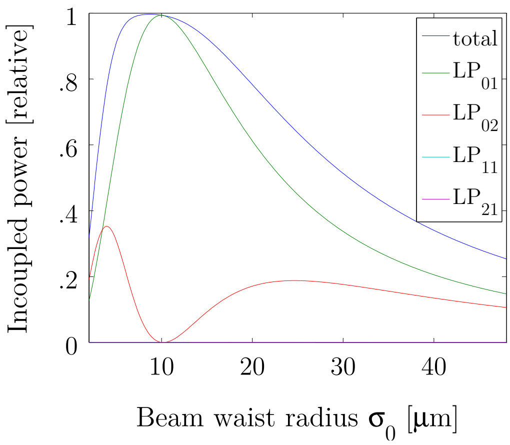

Figure 10: Modal coupling efficiency η_{lm} depending on the beam waist radius of the incident Gaussian beam σ_0 with phase plate $\boxed{0}$.

A more accurate estimation for the refractive index of the monolithic phase plate material, compared to the first quite rough guess prior to the first manufacturing of a phase plate, yielded $n_{\text{PDMS}} \approx 1.43$. Therefore for the simulation in addition to the perfect value of $\Delta\Phi = 180°$, also $\Delta\Phi = 144°$ was taken into account. The latter value originated from the downward estimation that $n_{\text{PDMS}} \approx 1.40$, together with the knowledge that the difference in the thickness of the phase plate was $d = 1064\,\text{nm}$.

For a phase plate like $\boxed{1}$ the azimuthal symmetry is broken. For $\Delta\Phi = 180°$ the symmetry of the incident beam is changed exactly to the one of the LP_{11}-mode and thus independent of the beam waist radius of the incident beam only LP_{11} is excited, as shown in figure 11.
The maximal amount of incoupled relative to the incident energy is 72.9 % for $\sigma_{\text{max}} = 12.7\,\mu\text{m}$.

This means that even in the best aligned setup more than a quarter of the incident energy is lost! This loss results from the missing alignment of the amplitude profile.

For $\Delta\Phi = 144°$ LP_{01} and LP_{02} are excited as well, which can be explained by considering the presence of an unperturbed Gaussian beam in the incident beam, as described in section 2.5 on page 11. LP_{02} however for this setup is excited with a negligible percentage of less than $\tilde{\eta}_{02} = 0.4\,\%$ around the maximum of the coupling efficiency for LP_{11} [again $\sigma_{\max} = 12.7\,\mu\text{m}$]. LP_{21} is not excited at all; this is no surprise, as the overlap integrals of a LP_{2m}-mode with a Gaussian beam as well as with a Gaussian beam shaped by phase plate $\boxed{1}$ are zero.

Although the overall amount of energy coupled into the fiber at the maximum of η_{11} for $\Delta\Phi = 144°$ is bigger [75.2 %] compared to a phase-plate $\boxed{1}$ with $\Delta\Phi = 180°$ [72.9 %], the amount of energy in LP_{11} is smaller [65.9 % instead of 72.9 %]. At the same time the ratio of LP_{11} in the incoupled beam [$\tilde{\rho}_{11}^2$] drops from 100 % for $\Delta\Phi = 180°$ to 87.7 % for $\Delta\Phi = 144°$.

Because by changing $\Delta\Phi$ only the magnitude of the perfectly adapted Gaussian beam varies, it is obvious that the course of the incoupling efficiency over σ_0 doesn't vary at all; only the amplitude changes corresponding to $\tilde{\rho}_l^2 = \frac{1}{2}\left[1 - \cos(\Delta\Phi)\right]$ [see section 2.5 on page 11].

For both $\Delta\Phi$ only one maximum of the total incoupled energy exists, which in both cases is very near to the maximum of η_{11}.

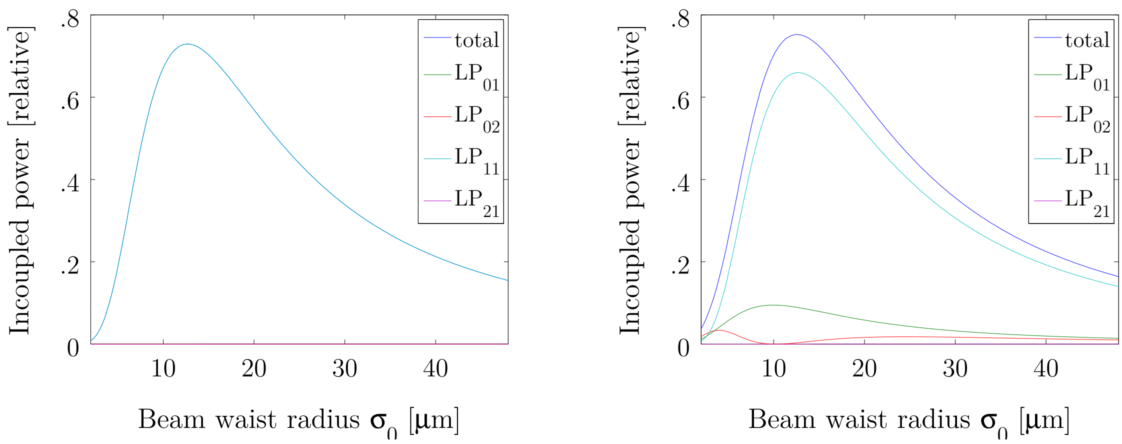

Figure 11: Modal coupling efficiency η_{lm} depending on the beam waist radius of the incident Gaussian beam σ_0 with phase plate $\boxed{1}$ and $\Delta\Phi = 180°$ and $\Delta\Phi = 144°$ respectively.

What has been said for phase plate $\boxed{1}$ with respect to LP_{11} now holds for phase plate $\boxed{2}$ with respect to LP_{21} as well, at least qualitatively [compare figure 12].

Quantitatively for $\Delta\Phi = 180°$ the maximum of η_{21} is even smaller with 67.2 % [for $\sigma_{\max} = 15.1\,\mu\text{m}$]; i.e. the loss in the best adjusted setup is nearly a third. This loss again originates from the misalignment of the amplitude profile of the incident beam E_{in}.

For $\Delta\Phi = 144°$ the maxima [again $\sigma_{\max} = 15.1\,\mu\text{m}$] are even smaller compared to the setup with phase plate $\boxed{1}$ as well; the maximal incoupled total energy is 69.6 % of the incident and then the purity of LP_{21} is decreased to 87.4 %.

This as well is understandable by a superposition of an undisturbed and a phase-profile-adapted Gaussian beam.

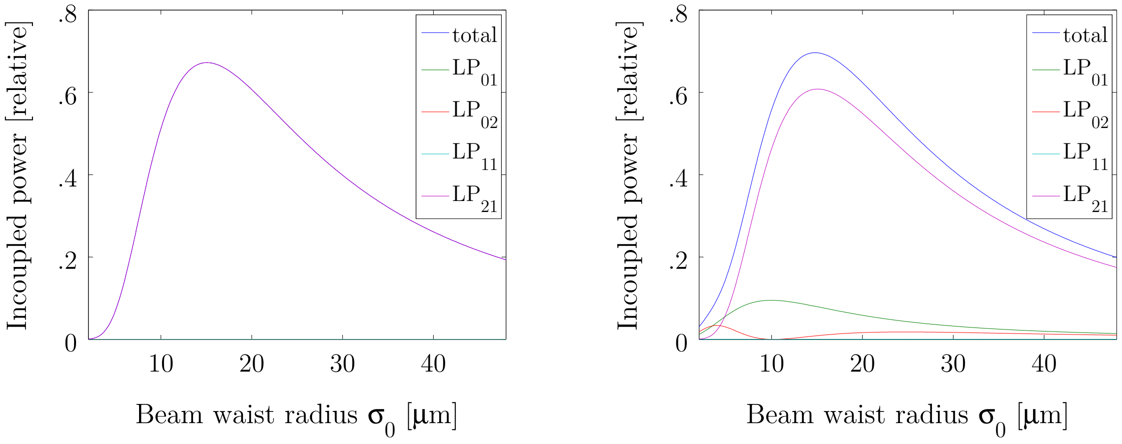

Figure 12: Modal coupling efficiency η_{lm} depending on the beam waist radius of the incident Gaussian beam σ_0 with phase plate $\boxed{2}$ and $\Delta\Phi = 180°$ and $\Delta\Phi = 144°$ respectively.

The radii of maximal incoupling efficiency for each phase plate are not affected by the phase shift $\Delta\Phi$. This again is understandable by the superposition of two identical Gaussian beams with respective phase profiles and different amplitudes, as the $\Delta\Phi$-change only alters the ratio of the perfectly adapted gaussian beam and doesn't affect it's radius.

4.3. Free Space Distance ζ

The LP-modes are weak guiding fiber- and not free space modes; i.e. while propagating through free space, the profiles inevitably change. Especially at the sharp edges in the phase profile diffraction will occur. Thus the distance ζ between the phase-shaping element and the fiber input plane should be minimal. This is the reason for investigating this monolithic setup of fiber and phase plate instead of one with the phase plate far away from the fiber input facet.

Therefore in the numerical setup the incident gaussian beam was modified by the phase plate not at its waist but ζ before it. Then it was numerically propagated by ζ and eventually the overlap integral η_{lm} with the fiber modes were determined. The results for the optimal Gaussian beam radius $\sigma_{\max}$, the total energetic incoupling ratio $\frac{P_{\text{incoupled}}}{P_{\text{in}}}$ and the energetic ratio for the desired mode $\tilde{\rho}_{lm}^2$ in the incoupled beam E in the fiber are displayed for phase plate $\boxed{1}$ in figure

13 and for phase plate $\boxed{2}$ in figure 14.

In both figures the same situations as described in the previous section are displayed for $\Delta\Phi = 180°$ and $\zeta = 0\,\mu m$. The bigger ζ, the smaller σ_{max} becomes, i.e. the phase shifted gaussian beam diverges, allthough the undisturbed beam was still before its waist position. For both investigated phase plates σ_{max} decreases slowly at first [$\zeta < 150\,\mu m$], then falls quite rapidly and finally decreases further asymptotically. For distances of ζ bigger than 750 µm no calculations have been made, as in the experimental setup the distance between phase plate and fiber input facet was definitly smaller than this.

The change in σ_{max} from $\zeta = 0\,\mu m$ to 750 µm is not as big for $\boxed{1}$ [6.1 µm] as for $\boxed{2}$ [10.7 µm]. This means, a Gaussian beam modified by the phase plate $\boxed{2}$ diverges much faster in free space than one modified by the phase plate $\boxed{1}$.

As displayed in figure 13, the amount of incoupled energy varies for the phase plate $\boxed{1}$ between 73.8 % and 65.1 % and shows a local minimum at $\zeta = 240\,\mu m \pm 10\,\mu m$; the global maximum is at $\zeta = 1\,\mu m \pm 1\,\mu m$, i.e. slightly bigger than zero. The free space propagation leads to a smoothing of the amplitude profile and adjusts the incident beam this way more to the LP_{11}-mode. The difference in the incoupled energy however is quite small.

For the phase plate $\boxed{2}$ [see figure 14] the amount of incoupled energy varies between 68.6 % and 41.1 % and shows a local minimum at $\zeta = 200\,\mu m \pm 10\,\mu m$; the coupling efficiency thus, as shown in the previous section for $\zeta = 0\,\mu m$, is worse for phase plate $\boxed{2}$ compared to phase plate $\boxed{1}$. The global maximum is at $\zeta = 1\,\mu m \pm 1\,\mu m$. This is, because of the smoothing of the amplitude profile during free space propagation, again slightly bigger than zero.

$\tilde{\rho}_{lm}^2$ of the desired mode can for both phase plates be kept above 99.9 % for $\zeta \in [0\,\mu m, 750\,\mu m]$ and $\Delta\Phi = 180°$. That means during a free space propagation smaller than 1 mm the phase profiles do not change, only the amplitude profiles vary.

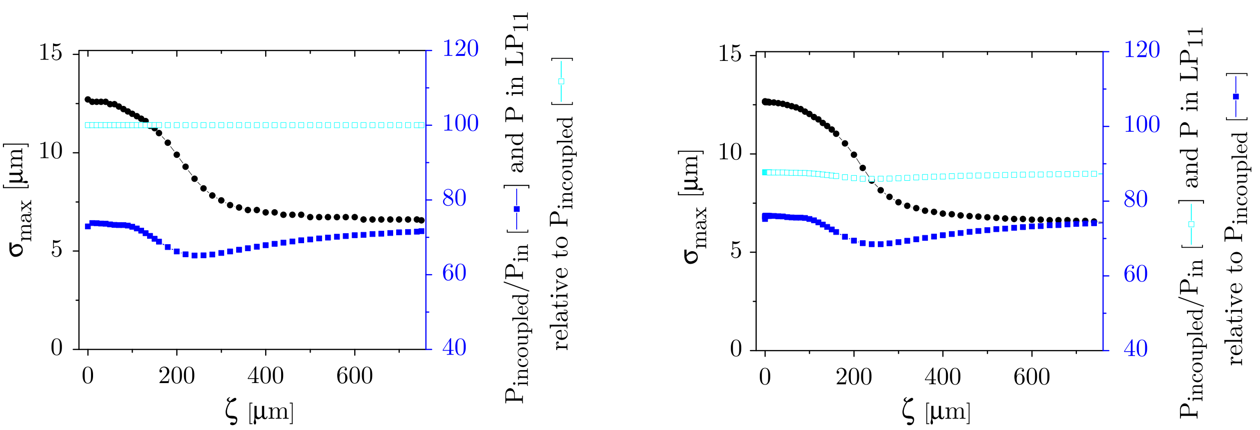

Figure 13: σ_{max}, $\frac{P_{incoupled}}{P_{in}}$ and $\tilde{\rho}_{11}^2$ over ζ using the phase plate $\boxed{1}$ with $\Delta\Phi = 180°$ and $\Delta\Phi = 144°$ respectively.

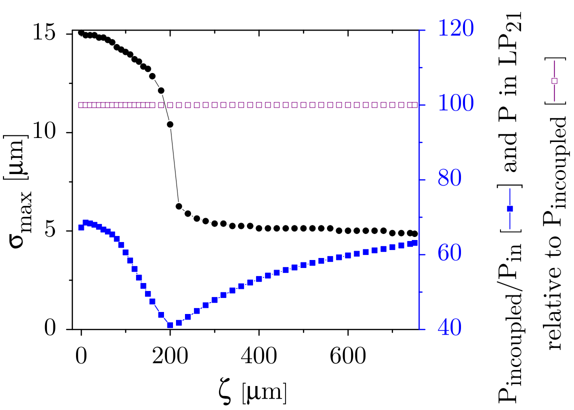

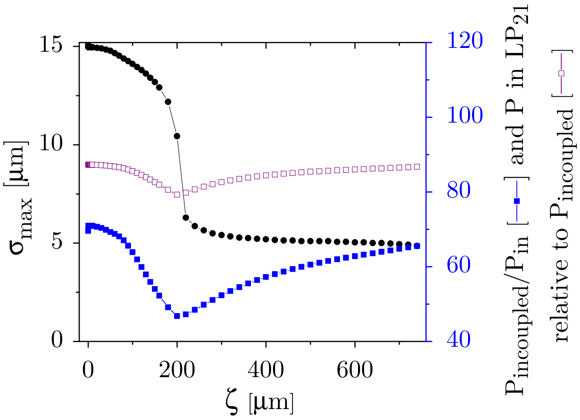

Figure 14: $\sigma_{\max}$, $\frac{P_{\text{incoupled}}}{P_{\text{in}}}$ and $\tilde{\rho}_{21}^2$ over ζ using the phase plate $\boxed{2}$ with $\Delta\Phi = 180°$ and $\Delta\Phi = 144°$ respectively.

For $\Delta\Phi = 144°$ the results are very similar:

The numerically inscribed beam waist diameter for maximal coupling efficiency in the respective desired mode $\sigma_{\max}$ differed for both phase plates less than 0.1 µm from $\sigma_{\max}$ for $\Delta\Phi = 180°$. As long as the propagation of the light is linear, which it was assumed at all times, $\sigma_{\max}$ should be independent of $\Delta\Phi$, as $\Delta\Phi$ influences only the ratio of the best adapted beam in the incoming field E_{in}.

The amount of incoupled energy was slightly bigger [up to 4 %], because of the excitation of LP_{01} and LP_{02}. Since at the same time the attenuation of the desired mode was not too strong, this led to slightly more energy being coupled into the fiber.

If the free-space distance between the phase plate and the fiber input facet is greater than 0 µm, then the purity of the desired mode for $\Delta\Phi \neq 180°$ is worse than for $\zeta = 0$ µm. This means the values determined for $\zeta = 0$ µm represent the best possible values in regard to the purity of the desired mode.

4.4. Transversal Displacement of the Incident Beam

Finally the dependence of the modally resolved coupling efficiency η_{lm} on the displacement of the incident beam in the transversal plane is investigated. Therefore a perfect monolithic setup [$\zeta = 0$ µm], a phase plate phase shift of $\Delta\Phi = 180°$ and an incident Gaussian beam of adapted size are assumed; the results are shown in figures 15 to 17.

The different scales in the coloring of the figures should be noted! As mentioned above, the maximal coupling efficiency becomes smaller from phase plate $\boxed{0}$ over $\boxed{1}$ to $\boxed{2}$.

Because some of the power distributions shown in figures 15 to 17 might seem similar to modal intensity distributions, it shall be emphasized that quite contrary the power in each mode group depending on the transversal displacement of the incident Gaussian beam is displayed.

As a quantitative measure for the sensitivity of this setup on the displacement of the incident Gaussian beam the full width at half maximum for the incoupled intensity of the respective desired mode was chosen; the values are shown in table 2.

Table 2: Full width at half maximum for the respective desired mode in the monolithic setup.

	$\boxed{0}$	$\boxed{1}$	$\boxed{2}$
$\Delta\Phi = 144°$	16.6 µm	19.2 µm	24.6 µm
$\Delta\Phi = 180°$		18.2 µm	24.6 µm

It is noteworthy that all of these values are smaller than the respective diameter of the incident Gaussian beam [$\boxed{0}$: $2\sigma_{\max} = 19.9\,\mu\text{m}$, $\boxed{1}$: $2\sigma_{\max} = 25.4\,\mu\text{m}$, $\boxed{2}$: $2\sigma_{\max} = 30.2\,\mu\text{m}$]. To put this in perspective, it is mentioned that the fiber core diameter is $2a = 24.5\,\mu\text{m}$.

By considering that, while the desired mode is exited more weakly by a displacement of the incident beam, other modes are excited stronger, it is apparent that the purity of the desired mode has to decrease even faster. Thus a good adjustment of the setup is essential for a strong excitation of only the desired mode.

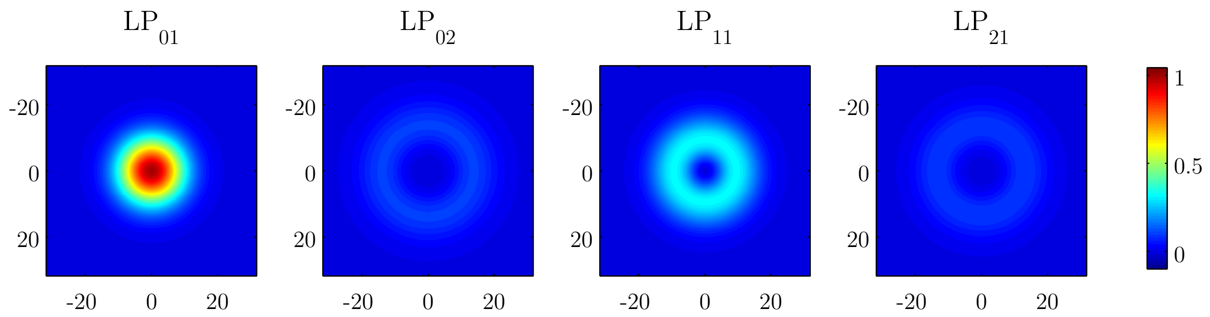

Figure 15: η_{lm} with phase plate $\boxed{0}$ and a beam with $\sigma_0 = 9.97\,\mu\text{m}$; dimensions in µm.

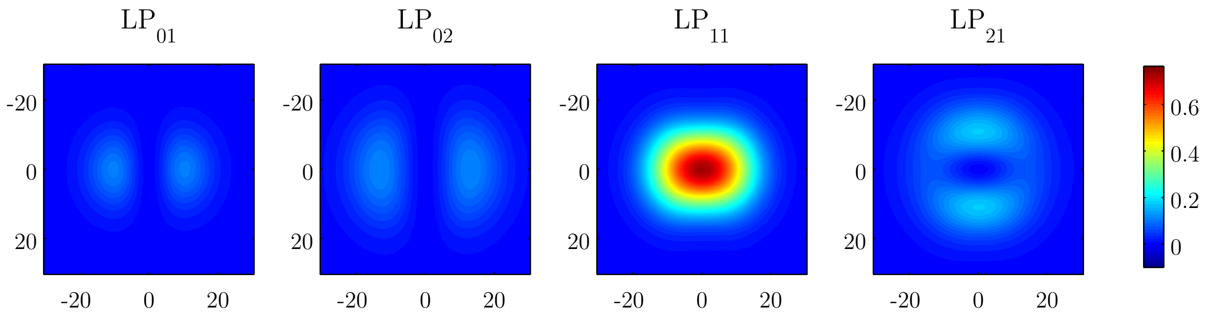

Figure 16: η_{lm} with phase plate $\boxed{1}$ with $\Delta\Phi = 180°$ and a beam with $\sigma_0 = 12.7\,\mu m$; dimensions in µm.

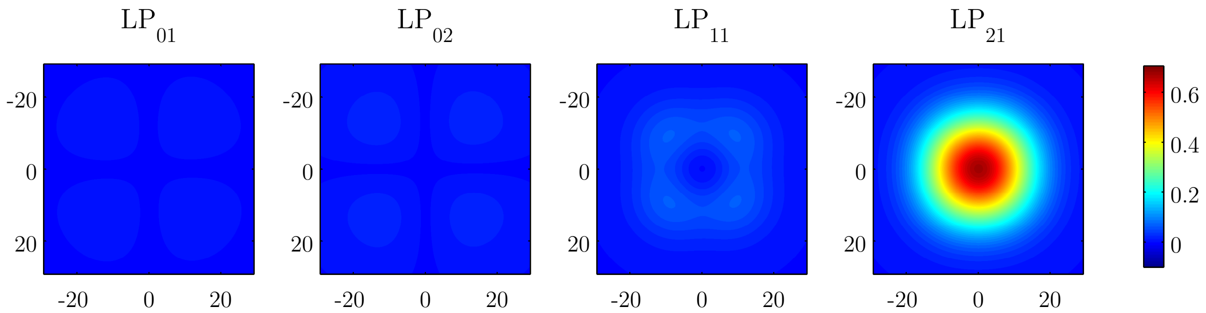

Figure 17: η_{lm} with phase plate $\boxed{2}$ with $\Delta\Phi = 180°$ and a beam with $\sigma_0 = 15.1\,\mu m$; dimensions in µm.

In order to adjust an experimental setup pertaining to the transversal displacement of the incident beam, the fact that the total incoupled energy does not have to be maximal with a centered beam has to be considered. However by knowing the other paramters [beam size σ_0, phase shift $\Delta\Phi$, free space propagation distance ζ], which are defined by the setup, one can numerically simulate the situation quickly and thus make it possible to adjust the incident beam transversally by a simple power measurement behind the fiber.

5. Experiment

In this section the experimental results achieved by the setup described in section 3 will be presented. After comparing these to the numerical predictions from section 4.4, a short comparison to a setup, where phase plate and fiber are much more distant from each other, will be given.

5.1. Results

The experimental analyses have all been made resolved in even and odd modes as well as in the linear polarizations [under 0° and 90° relative to the polarization state of the laser].

The distribution of incoupled energy between the even and odd modes in one mode group was, considering some experimental imperfections, in good agreement with the numerical predictions. These however were not displayed in this paper, because of the aforementioned symmetry of the fiber and the arbitrariness of the orientation of even and odd modes.

The distribution of the incoupled energy between the two orthogonal polarization states featured [at the best adjusted position of the experiments] ratios shown in table 3. This is due to the modal birefringence [27], which obviously varies in its effect for the LP-modes E_{lm}^{p} with different l. Especially the LP_{01}-mode, which showed to be quite strong under 0°-polarization, was much weaker even relative to the LP-modes with $l = 1$ or $l = 2$ under 90°-polarization.

Table 3: Measured energy ratios between the different polarization states [0° : 90°].

$\boxed{0}$	> 20 : 1
$\boxed{1}$	10 : 1
$\boxed{2}$	2 : 1

The dependencies of the modal coupling efficiency on the Gaussian beam waist radius σ_0, the free space between phase plate and fiber input facet ζ and the phase plate phase shift $\Delta\Phi$, which in section 4 were numerically investigated, weren't experimentally tested. For σ_0 the optimal value was chosen and ζ and $\Delta\Phi$ were fix for the setup and could not be changed easily.

The dependence of the modal power in the fiber on the transversal displacement of the Gaussian beam for the phase plate $\boxed{0}$ is depicted in figure 18. The very good agreement with the numerical predictions from section 4 [figure 15 on page 22] is apparent. The numerically perfect annuli for LP_{02}, LP_{11} and LP_{21} however are all cut off on one side; this indicates a slight tilt of the incident beam against the fiber front facet.

The maximum purity of LP_{01} and the coupling efficiency of this setup will be discussed later [page 27], in order to compare the characteristics of all investigated phase plates with each other.

The short line of higher intensity in one of the lower lines of the diagrams measured with the hexapod doesn't mean anything: Because the capture of each diagram took approximately ten minutes and all lights and computer monitors were turned off in the laboratory, I left for that time. Often then I came back a little to early, so that the ceiling illumination from the corridor outside the laboratory disturbed the measurement. But from this, it is now visible that the diagram was captured in horizontal lines from the top to the bottom; each line was rasterized in the same orientation.

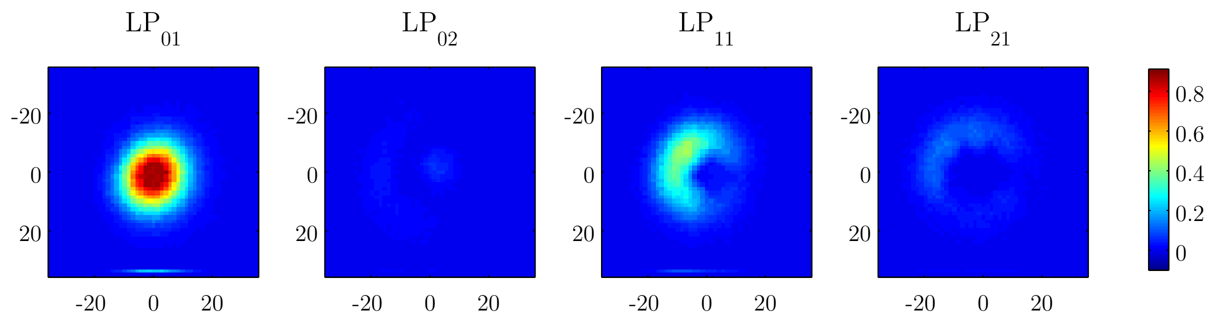

Figure 18: Experimental modal coupling efficiency $\tilde{\eta}_{lm}$ for phase plate $\boxed{0}$ depending on the transversal displacement of the incident beam; dimensions in µm.

The results for phase plate $\boxed{1}$ are shown in figure 19. It is evident that there are differences to the numerical simulation in section 4.4 [figure 16 on page 23]. Nevertheless LP_{11} is still the strongest excited mode in the fiber for the optimal coupling position.

To reproduce the experimental results numerically several approaches have been made; by choosing a vertical [corresponding to figure 5 on page 11] displacement of the phase plate relative to the center of the fiber of about 2 µm, setting the phase shift of the phase plate to $\Delta\Phi = 144°$ and the beam waist radius to $\sigma_0 = 15\,\mu m$, the measured profile can be approximated. The most important parameter here is the displacement of the phase plate.

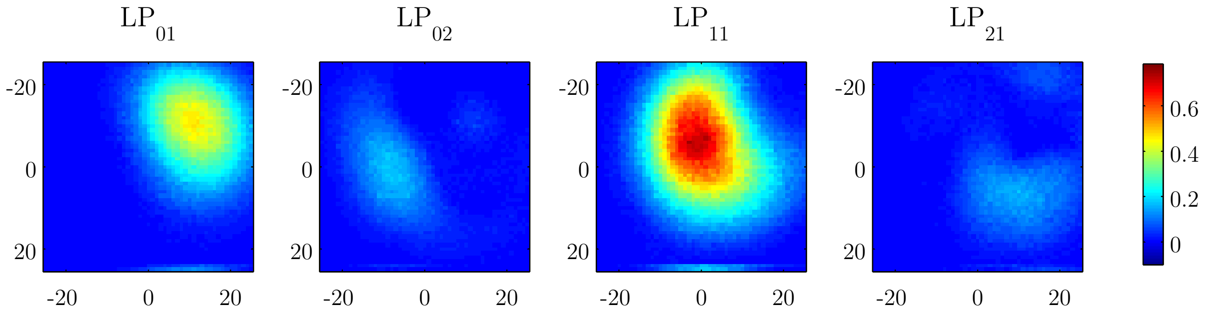

Figure 19: Experimental modal coupling efficiency $\tilde{\eta}_{lm}$ for phase plate $\boxed{1}$ depending on the transversal displacement of the incident beam; dimensions in µm.

For phase plate $\boxed{2}$ the measurement with the hexapod yielded results that again indicate a displacement of the phase plate [this time diagonally [corresponding to figure 5 on page 11] by 3 µm]. Hence the resemblance to the simulation was quite poor and therefore the measurement is not displayed here.

Chronologically before the fully automated measurement with the hexapod a manual scan has been performed. This manual measurement yielded the results shown in figure 20. Because these scans show LP_{21} as the most dominant mode by far in correspondence with the numerical simulation shown in figure 17 on page 23 and because the course of the spatial dependence is also very similar, the phase plate is assumed to have shifted during the installation of the hexapod into the setup. This is not unlikely, as the fiber had to be taken out of the setup and put back in, in order to install the hexapod, and the phase plate was only fixated by adhesive forces on a metal mount around the fiber.

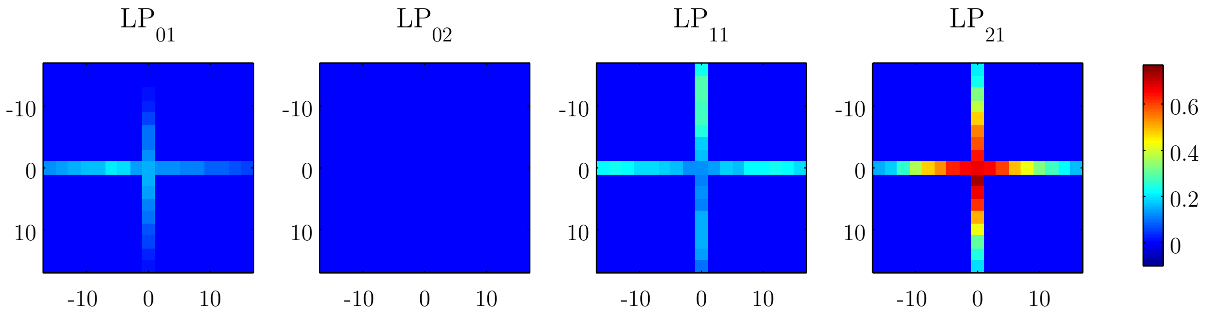

Figure 20: Experimental modal coupling efficiency $\tilde{\eta}_{lm}$ for phase plate $\boxed{2}$ depending on the transversal displacement of the incident beam; dimensions in µm.

Reading off the relative energetic ratios of the modes $\tilde{\rho}_{lm}^2$ in the previously shown experimental results at the maximum of the desired mode's coupling efficiency, one obtains the results shown in figure 21. For comparison the numerical results for an respectively adapted setup [see the following paragraphs] are shown in figure 21 as well.

The numeric value of $\tilde{\rho}_{01}^2$ for the phase plate $\boxed{0}$ differs by 2.1 % from the theoretical prediction; for the latter a too large beam waist of $\sigma_0 = 13.0\,\mu\text{m}$ instead of 9.97 µm was assumed. Considering $M_{\text{eff}}^2 = 1.21$ for the used laser and a tilt of the incident beam against the fiber front facet, the agreement of theory and experiment is very good.

For phase plate $\boxed{1}$ the numeric value of $\tilde{\rho}_{11}^2$ differs by 7.5 % from the theoretical prediction; here an off-centering of the phase plate of 1 µm, a phase shift $\Delta\Phi = 144°$ and a perfectly adapted Gaussian beam waist radius of $\sigma_0 = 12.7\,\mu\text{m}$ were assumed. It should be noted that different parameters can lead to the same results and therefore the reconstruction purely from the modal energy ratios on all possible parameters is not unambiguously possible. The experimental results for phase plate $\boxed{1}$ though could be reconstructed numerically with the above mentioned reasonable parameters.

Phase plate $\boxed{2}$ shows a very strong resemblance of numerical and experimental results; the maximal difference is 0.6 % for LP_{21}. For the simulation a slightly too small beam waist of $\sigma_0 = 12.0\,\mu\text{m}$ [instead of 15.1 µm], a phase shift of $\Delta\Phi = 144°$ and an off-centering of the phase plate of approximately 2 µm were assumed.

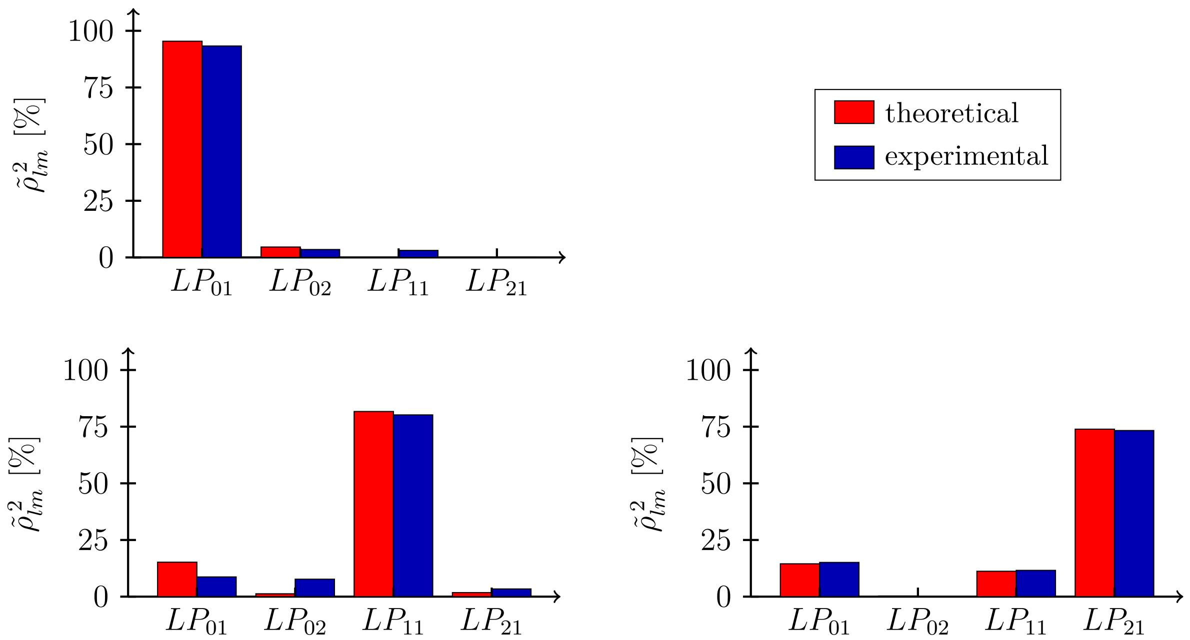

Figure 21: Diagram of the incoupled theoretical [left bars; best adjusted parameters] and experimental [right bars] modal energy ratios $\tilde{\rho}_{lm}^2$ for phase plate $\boxed{0}$ [upper left], $\boxed{1}$ [lower left] or $\boxed{2}$ [lower right] in a monolithic setup.

The most important parameters, in order to optimize the setup, thus are the transversal displacement of the phase plate relative to the fiber and the phase shift of the phase plate $\Delta\Phi$. Regardless of these possible improvements, the primary excitation of higher order modes already could be experimentally demonstrated.

5.2. Comparison with a Non-Monolithic Setup

One Phase plate in free space in front of a fiber input facet with at least some centimeters between them, i.e. a non-monolithic setup, has been used several times [e.g. [6, 7, 9]]. Therefore such setups are chosen as a reference to the monolithic setup. The measurements have been performed with exactly the same setup, only the monolithic phase plate was exchanged with a separate one. All the same numeric and experimental investigations have been made. Because these measurements only serve as a comparison, the numerical and experimental results therefor are shown in the appendix on pages i and ii.

It should be noted that for phase plate $\boxed{0}$ the monolithic and the free space setup are equivalent; at least theoretically.

The refractive index of the photoresist used for the manufacturing of the free space phase plate was known, therefore $\Delta\Phi$ was very near to 180°. The comparison of the experimental results with simulations of optimal parameters [beam, phase plate and fiber concentric, phase shift $\Delta\Phi = 180°$] can be seen in figure 22. Considering measurement errors from the camera, a small tilt of the incoming beam and again the $M^2_{\text{eff}} = 1.21$ of the laser, these differences of measurement and simulation don't seem too big.
The effects of a nearly optimal phase shift are visible. The purity of the respectively desired mode might not be at the numerically predicted 100 %, but is already quite high with 88.7 % in the worst case [for phase plate $\boxed{1}$]. Thus, in comparison with the results for the monolithic setup [see figure 21 on page 27], where $\Delta\Phi = 144°$ was assumed, the importance of the correct phase shift $\Delta\Phi$ is apparent.

The dependence of the energy, which is coupled into the fiber, on the transversal displacement of the fiber relative to the phase shifted beam numerically showed to be at least twice as sensitive for the non-monolithic setup; the FWHM is for phase plate $\boxed{1}$ 8.2 µm instead of 18.2 µm and for phase plate $\boxed{2}$ 8.8 µm instead of 24.6 µm wide.

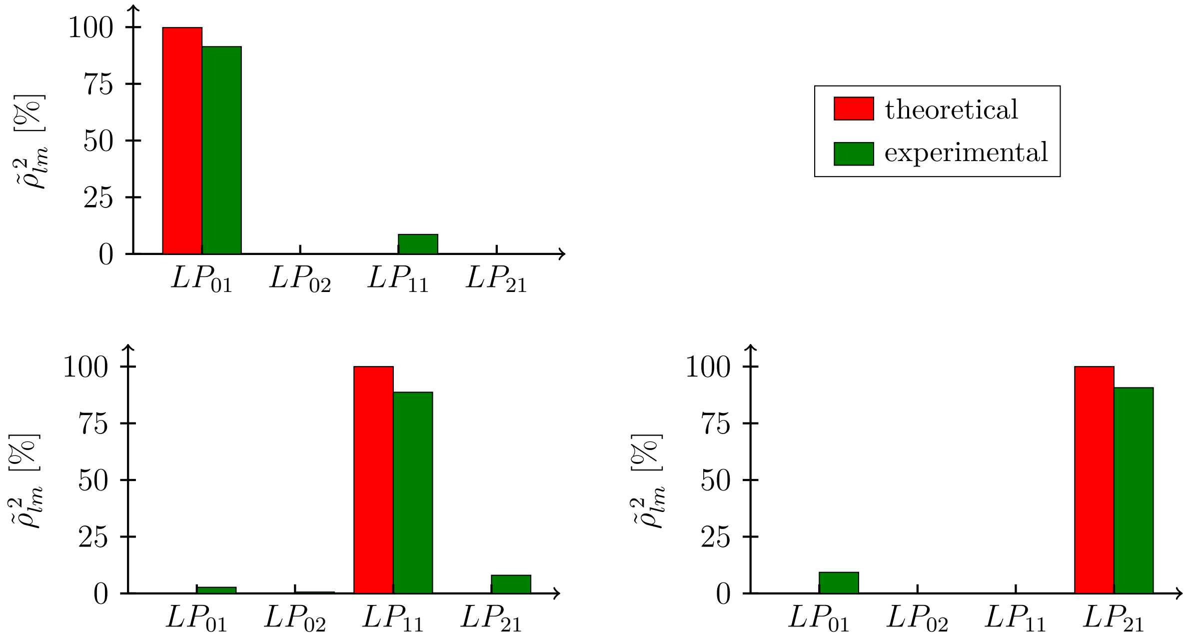

Figure 22: Diagramm of the incoupled theoretical [left bars; optimal setup assumed] and experimental [right bars] $\tilde{\rho}^2_{lm}$ for $\boxed{0}$ [upper left], $\boxed{1}$ [lower left] and $\boxed{2}$ [lower right] in a non-monolithic setup.

In figure 23 the amount of the total incoupled relative to the incident power, as seen in the experiments, is depicted. These values were recorded at optimized coupling positions. Apparently the values for the monolithic setup are higher. One reason for this is that the phase shift $\Delta\Phi$ differed more from the optimal value of $\Delta\Phi = 180°$ for the monolithic setup and thus other modes could be excited, too; mainly LP_{01}. Yet the measured differences between the free space and the monolithic setups are bigger than explicable hereby and at least the experiments for phase plates $\boxed{0}$ and $\boxed{2}$ in the monolithic setup [see figures 18 on page 25 and 20 on page 26] showed, that the respective desired modes are very dominant. Therefore the main reason for the lower coupling efficiency of the non-monolithic setup is assumed to be the relatively long propagation distance between the free space phase plate and the fiber front facet, over which the phase shaped beam changes its amplitude profile.

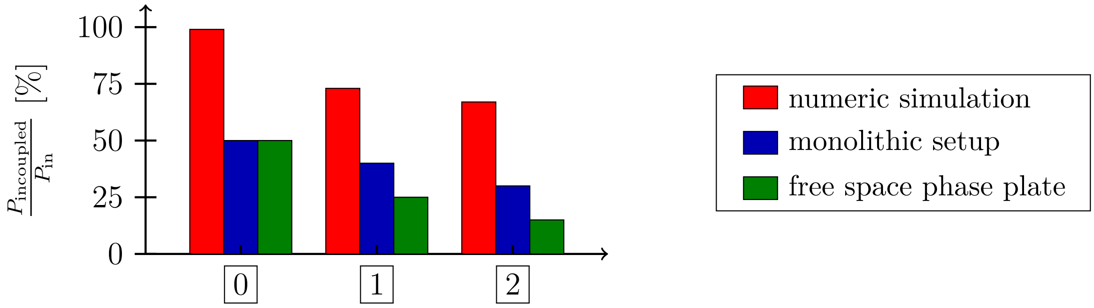

Figure 23: Diagram of the experimentally determined coupling efficiencies $\frac{P_{\text{incoupled}}}{P_{\text{in}}}$ for the monolithic setup [middle bars; $\Delta\Phi = 144°$] and the non-monolithic setup [right bars]. For comparison the numerically calculated expectations for the best adjusted case are given as well [left bars].

6. Conclusion and Outlook

For the selective excitation of higher order modes in few mode fibers [FMF] several different approaches already have been proposed and investigated [e.g. [6, 8, 9, 28]]. These however need a lot of room for the setup, are inefficient and/or can be quite expensive. To overcome these limitations, the new approach for this investigation was to use a very compact setup of a passive binary phase plate and a FMF [called "monolithic"].

In order to evaluate the theoretical capabilities of the investigated approach, numerical simulations have been performed prior to the experiments. For ideally manufactured phaseplates and optimal coupling conditions the numerical simulations showed an achievable mode purity of 100 % for all investigated phase plates. Only if the phase shift $\Delta\Phi \neq 180°$, then the waist size of the incident beam σ_0 or the distance between the phase plate and the fiber ζ affected the achievable mode purity. The coupling efficiency into the fiber for every phase shift $\Delta\Phi$ got worse though for bigger distances between phase plate and fiber ζ.

The experimental results showed a good agreement with the simulations. Yet mainly because of the imperfect phase shift $\Delta\Phi$ of the phase plates used, differences in the achieved mode purity occured. The measured values for the modal energy ratios were $\tilde{\rho}_{01}^2 = 93.3\,\%$ for the phase plate adjusted to LP_{01}, $\tilde{\rho}_{11}^2 = 80.2\,\%$ for the phase plate adapted to LP_{11} and $\tilde{\rho}_{21}^2 = 73.3\,\%$ for the phase plate adjusted to LP_{21}.

In comparison with a setup with a free space phase plate, which's phase shift was much closer to the optimal value of $\Delta\Phi = 180°$, it already could be shown experimentally that the coupling efficiency of the monolithic setup is higher: For the phase plate adapted to LP_{11} the coupling efficiency for the monolithic setup was much higher than for the free space setup with approximately 40 % in comparison to 25 %. For the phase plate adapted to LP_{21} the respective values were even more diverse with 30 % in coparison to 15 %.

These results show that the monolithic setup used in this study is a promising approach for an efficient excitation of one higher order mode, while requiring minimal room. Based on these properties and because the guidance of higher order modes in a fiber is much stronger affected by external perturbations [e.g. temperature, pressure or stress] compared to lower order modes, it seems reasonable to use this setup for a sensor. The measurement, knowing what mode is guided by the fiber, can then be simplified to the measurement of the power emitted from the fiber.

However the dependence of a lot of parameters has been examined in this study [namely the beam waist radius of the incident beam, the displacement of the incident beam transversal to the incoupling plane, the phase shift of the phase plate and the free space distance between the phase plate and fiber], for a further understanding of the setup more parameters remain. The most important are the displacement of the phase plate relative to the concentric position with the fiber and a tilt of the incident beam realtive to the fiber input facet.

For an even more sophisticated understanding investigations resolved in the polarization and the orientation of the modes can be undertaken. In the conducted experiments, where the disturbances were kept to a minimum, these distinctions have already been recorded. In order to understand the effects of disturbances [like modal birefringence [9] or the influence of bends in and pressure on the fiber [as investigated in [4, 5]]] further experiments and numeric simulations need to be made. These are necessary if one wants to use this setup for a sensor.

However before these properties are going to be experimentally investigated in the future, the phase shift of the phase plates should be optimized and the phase plate fixated much firmer relative to the fiber.

Allthough the approach of a monolithic phase plate and fiber setup has mainly been investigated for the use in a fiber sensor, it shall be noted, that the same principle of selective higher mode excitation also can be used in other applications; e.g. in fiber lasers or in communication fibers.

A. Additional Graphs

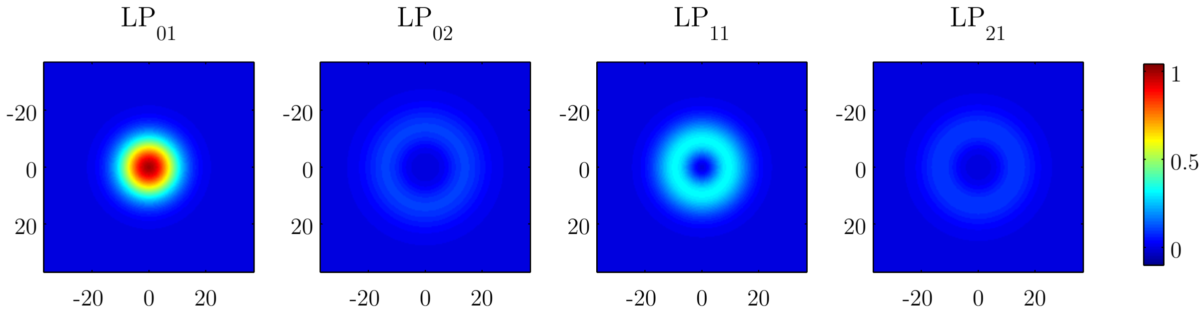

Figure 24: Numerically calculated coupling efficiencies η_{lm} for phase plate $\boxed{0}$, which theoretically is the same as using no phase plate at all, in the free space setup with $\Delta\Phi = 180°$ and a beam with $\sigma_0 = 9.96\,\mu m$ dependent on the displacement of the fiber; dimensions in µm.

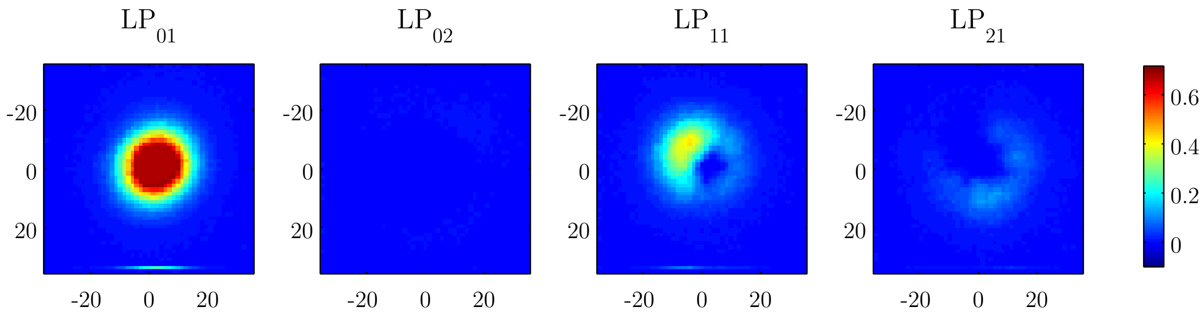

Figure 25: Experimentally determined coupling efficiencies normalized to the total incoupled power $\tilde{\eta}_{lm}$ without any phase plate and an optimally adjusted setup dependent on the displacement of the fiber; dimensions in µm.

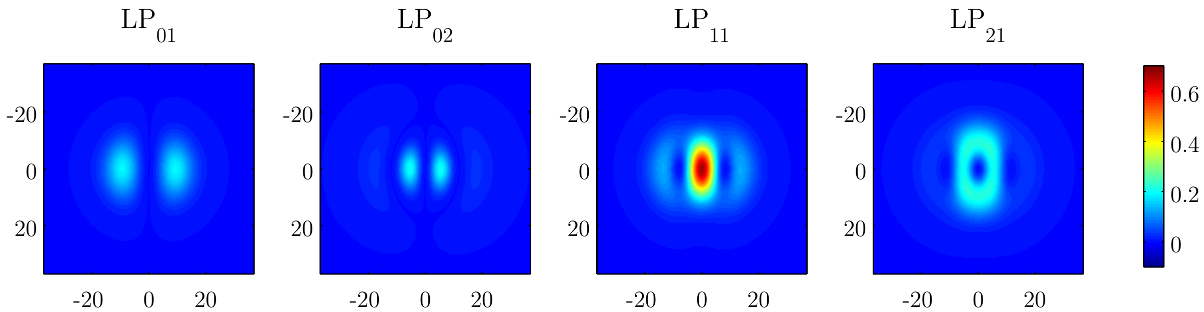

Figure 26: Numerically calculated coupling efficiencies η_{lm} for phase plate $\boxed{1}$ in the free space setup with $\Delta\Phi = 180°$ and a beam with $\sigma_0 = 9.97\,\mu m$ dependent on the displacement of the fiber; dimensions in µm.

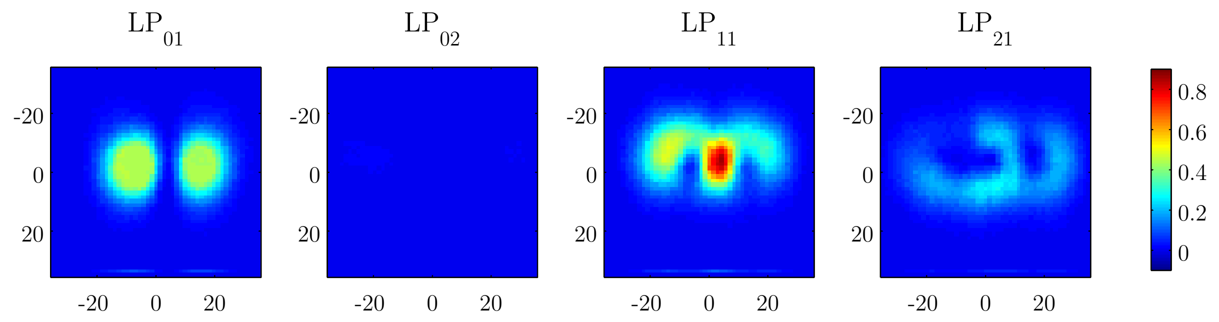

Figure 27: Experimentally determined coupling efficiencies normalized to the total incoupled power $\tilde{\eta}_{lm}$ for phase plate $\boxed{1}$ in the free space setup with $\Delta\Phi = 180°$ and an optimally adjusted setup dependent on the displacement of the fiber; dimensions in µm.

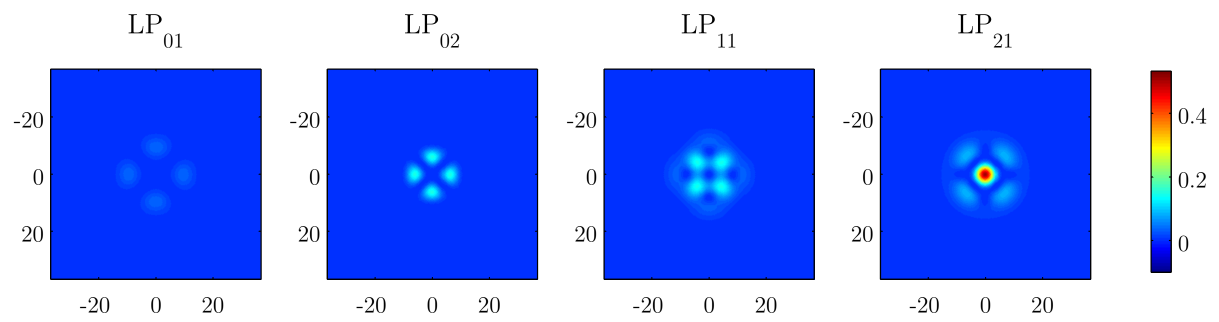

Figure 28: Numerically calculated coupling efficiencies η_{lm} for phase plate $\boxed{2}$ in the free space setup with $\Delta\Phi = 180°$ and a beam with $\sigma_0 = 9.97\,\mu\text{m}$ dependent on the displacement of the fiber; dimensions in µm.

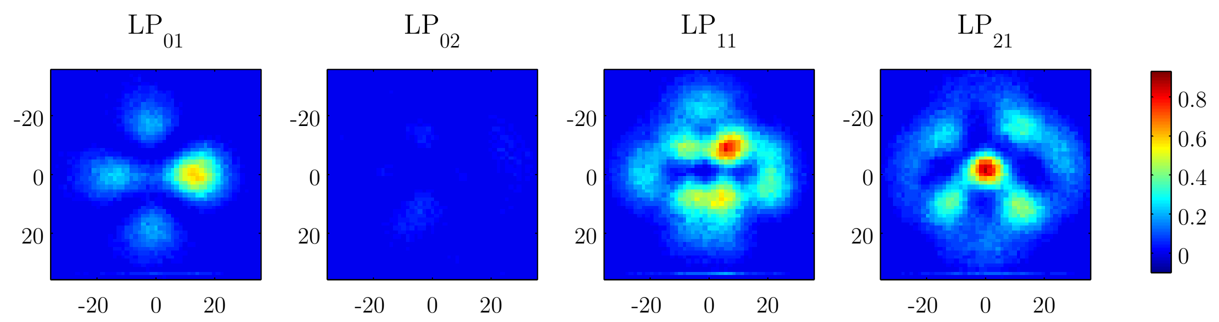

Figure 29: Experimentally determined coupling efficiencies normalized to the total incoupled power $\tilde{\eta}_{lm}$ for a phase plate $\boxed{2}$ in the free space setup with $\Delta\Phi = 180°$ and an optimally adjusted setup dependent on the displacement of the fiber; dimensions in µm.

B. References

[1] Y. e. Jeong, J. Sahu, D. Payne, and J. Nilsson, "Ytterbium-doped large-core fiber laser with 1.36 kw continuous-wave output power", Optics Express **12**, 6088–6092 (2004).

[2] B. Lee, "Review of the present status of optical fiber sensors", Optical Fiber Technology **9**, 57 – 79 (2003).

[3] B. Lee and Y. Jeong, "Interrogation techniques for fiber grating sensors and the theory of fiber gratings", Fiber Optic Sensors pp. 295–381 (2002).

[4] C. Schulze, A. Lorenz, D. Flamm, A. Hartung, S. Schröter, H. Bartelt, and M. Duparré, "Mode resolved bend loss in few-mode optical fibers", Opt. Express **21**, 3170–3181 (2013).

[5] C. Schulze, J. Wilde, R. Brüning, S. Schröter, and M. Duparré, "Measurement of effective refractive index differences in multimode optical fibers based on modal decomposition", (2014).

[6] G. Stepniak, L. Maksymiuk, and J. Siuzdak, "Binary-phase spatial light filters for mode-selective excitation of multimode fibers", Journal of lightwave technology **29**, 1980–1987 (2011).

[7] D. Flamm, C. Schulze, D. Naidoo, S. Schröter, A. Forbes, and M. Duparré, "All-digital holographic tool for mode excitation and analysis in optical fibers", Journal of Lightwave Technology **31**, 1023–1032 (2013).

[8] C. Schulze, "Laser beam characterization with holographic tools", Diploma thesis, FSU Jena (2014).

[9] J. von Hoyningen-Huene, R. Ryf, P. Winzer *et al.*, "Lcos-based mode shaper for few-mode fiber", Optics express **21**, 18097–18110 (2013).

[10] C. E. Webb and J. D. Jones, *Handbook of Laser Technology and Applications: Laser design and laser systems*, vol. 2 (CRC Press, 2004).

[11] J. D. Jackson, *Classical electrodynamics*, vol. 3 (Wiley New York etc., 1962).

[12] R. Winter and W. Wörstenfeld, *Das große Tafelwerk interaktiv* (Cornelsen, 2003).

[13] A. E. Siegman, *Lasers* (University Science Books, Sausalito, California, 1986), revised. ed.

[14] F. Lederer, "Theoretische Optik", Script, FSU Jena (2008).

[15] F. M. Mitschke, *Glasfasern: Physik und Technologie* (Elsevier, Spektrum Akademischer Verlag, 2005).

[16] National Communications System (U.S.). Technology & Standards Division and United States. General Services Administration Information Technology Section, *Telecommunications: Glossary of Telecommunication Terms*, Federal Standard (Government Institutes, 1997).

[17] D. Glodge, “Weakly guiding fibers”, Applied Optics (1971).

[18] T. Kaiser, “Field reconstruction in optical fibers by complete modal decomposition using computer-generated holograms”, Diploma thesis, Friedrich-Schiller-Universität Jena (2008).

[19] W. Thornburg, B. Corrado, and X. Zhu, “Selective launching of higher-order modes into an optical fiber with an optical phase shifter”, Optics letters **19**, 454–456 (1994).

[20] R. Ryf, S. Randel, A. H. Gnauck, C. Bolle, A. Sierra, S. Mumtaz, M. Esmaeelpour, E. C. Burrows, R.-J. Essiambre, P. J. Winzer *et al.*, “Mode-division multiplexing over 96 km of few-mode fiber using coherent 6 6 mimo processing”, Lightwave Technology, Journal of **30**, 521–531 (2012).

[21] J. Han, M. Sparkes, and W. O’Neill, “Controlling the optical fiber output beam profile by focused ion beam machining of a phase hologram on fiber tip”, (2014).

[22] L. Raddatz, I. White, D. Cunningham, and M. Nowell, “An experimental and theoretical study of the offset launch technique for the enhancement of the bandwidth of multimode fiber links”, Journal of Lightwave Technology **16**, 324 (1998).

[23] W. H. Lee, “Sampled Fourier transform hologram generated by computer”, Appl. Opt. **9**, 639–643 (1970).

[24] C. Rockstuhl, “Theoretische und experimentelle Untersuchungen zur Laserstrahlanalyse mit diffraktiven Korrelationsfiltern”, Diploma thesis, FSU Jena (2001).

[25] P. Gelszinnis, “Bestimmung der modalen Zusammensetzung bei der Feldeinkopplung von einer Single- in eine Multimodefaser”, (2011).

[26] A. B. Fallahkhair, K. S. Li, and T. E. Murphy, “Vector finite difference modesolver for anisotropic dielectric waveguides”, Journal of Lightwave Technology **26**, 1423–1431 (2008).

[27] H. Kogelnik and P. Winzer, “Modal birefringence in weakly guiding fibers”, Journal of Lightwave Technology **30**, 2240–2245 (2012).

[28] R. Brüning, “Analysis of optical vortex beams by means of hollographic correlation filters”, Master’s thesis, Friedrich-Schiller-Universität Jena (2013).

[29] T. Bätz, “Modellierung und Simulation optischer Strahlführungen”, Master’s thesis, Technische Universität Dresden (2012).

[30] M. Born and E. Wolf, *Principles of Optics: Electromagnetic Theory of Propagation, Interference and Diffraction of Light* (Pergamon Press, 1970), 4th ed.

[31] C.-L. Chen, “Excitation of higher order modes in optical fibers with parabolic index profile”, Applied optics **27**, 2353–2356 (1988).

[32] J. W. Goodman, *Introduction to Fourier optics* (Roberts and Company Publishers, 2004).

[33] L. Jeunhomme and J. Pocholle, “Selective mode excitation of graded index optical fibers”, Applied optics **17**, 463–468 (1978).

[34] R. W. Tkach, “Scaling optical communications for the next decade and beyond”, Bell Labs Technical Journal **14**, 3–9 (2010).

Versicherung der selbstständigen Erarbeitung und Anfertigung

Ich erkläre, dass ich vorliegende Arbeit selbständig und nur unter Verwendung der angegeben Hilfsmittel und Quellen angefertigt habe. Die eingereichte Arbeit ist nicht anderweitig als Prüfungsleistung verwendet worden oder in deutscher oder einer anderen Sprache als Veröffentlichung erschienen.

Seitens des Verfassers bestehen keine Einwände, die vorliegende Bachelorarbeit für die öffentliche Benutzung zur Verfügung zu stellen.

Jena, den 24. September 2014

Johannes Wilde